Research on vibration signal decomposition of cracked rotor-bearing system with double-disk based on CEEMDAN-CWT

Zhou, Wenjie; Jin, Xian; Ding, Lei; Ma, Ji; Su, Huihao; Zhao, An

DOI
10.1016/j.apacoust.2024.110254

Publication date
2025

Document Version
Final published version

Published in
Applied Acoustics

Applied Acoustics 227 (2025) 110254

Contents lists available at ScienceDirect

Applied Acoustics

journal homepage: www.elsevier.com/locate/apacoust

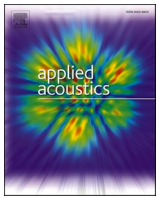

Research on vibration signal decomposition of cracked rotor-bearing system with double-disk based on CEEMDAN-CWT

Wenjie Zhou [a,*], Xian Jin [a], Lei Ding [a], Ji Ma [a], Huihao Su [a], An Zhao [b]

[a] School of Energy and Power Engineering, Jiangsu University, Zhenjiang 212013, PR China
[b] Department of Process & Energy, Delft University of Technology, Delft 2628 CD, the Netherlands

ARTICLE INFO

Keywords:
Rotor-bearing system
Multi-degrees of freedom (M−DoFs)
CEEMDAN-CWT method
Dynamic characteristics
Signal decomposition

ABSTRACT

In the actual working process, the source of vibration signal is not only the rotor itself, so the detected vibration signal will become complicated. This complex signal makes it difficult to accurately measure the existence of crack. In this paper, a novel method, which includes complete ensemble empirical mode decomposition with adaptive noise (CEEMDAN) and continuous wavelet transform (CWT), is proposed to analyze the cracked rotor-rolling bearing system. The CEEMDAN-CWT successfully separates the vibration signal of the rotor itself from the original signal and provides results similar to the simulation signal. At the speed below 2000 rpm, the 2X frequency difference between cracked rotor and healthy rotor in CEEMDAN-CWT spectrum is about 1, while the difference of FFT spectrum of original signal is about 0.6, which shows the superiority of the novel method in extracting rotor vibration signals from complex vibration signals.

1. Introduction

Two-stage or even multi-stage rotor-bearing systems are widely used in many fields, including water conservancy, aviation, and power generation. These systems consist of multiple stages of rotors and bearings, which are designed to transmit rotational forces and support loads in various industrial applications [1]. However, due to the harsh working environment faced by rotating machinery, cracks and other faults will inevitably occur in its components, and these faults will affect the stability of system operation [2–4]. As early as 1990 s, many scholars have paid much more attention to the cracked rotor system. For the most common transverse cracks, Wauer [5], Gasch [6] and Dimarogonas [7] observed that the existence of transverse cracks on the shaft caused the unusual vibration of the rotor system. However, traditional experiments can't meet the needs of theoretical research, so the development of theoretical model used to describe cracked rotor is constantly developed. Jun et al. [8] derived and presented equations of motion for a rotor with a breathing crack. Darpe et al. [9,10] introduced the concept of the Crack Closure Line (CCL) and determined the opening and closing states of the crack at any angle. Al-Shudeifat and Butcher [11] use two new functions to formulate the time-varying stiffness matrix of cracked elements. These new functions can be used to approximately describe the actual breathing mechanism of cracks. The stability of the system considering the crack depth and rotating speed is examined using Floquet theory [12]. Zhang and Li [13] developed coupled equations of motion in 6 degrees of freedom (6-DoFs) for a cracked rotor. They examined the effect of breathing behavior under various parameters. The results suggested that a rotor system with 6-DoFs allows a more accurate characterization of rotor vibration than a rotor system with only 4-DoFs. Spagnol et al. [14] investigated the shifting of the neutral axis in cracked rotors, demonstrating the potential of their proposed model in modeling and detecting cracks during the middle and later stages of rotor operation. Sinou and Denimal [15] proposed an advanced modeling technique based on kriging and Polynomial Chaos Expansion (PCE) to describe the breathing phenomena of cracks. Kushwaha and Patel [16] modeled the time-varying stiffness matrix by considering the area product moment. Then a simplified breathing function was proposed to describe the actual breathing transverse cracks.

In addition, many scholars pay attention to the vibration characteristics of cracked rotor-bearing system [17,18]. Fu et al. [19] explored the effects of interval uncertain parameters on the vibration of a rotor system with a transverse breathing crack, which consisted of two disks and an elastic shaft. Then a double-disk hollow-shaft rotor model was investigated [20]. Zhang et al. [21] proposed a multi-disk rod fastening rotor system, revealing that the dynamic characteristics of the system changed with the inclusion of the crack fault. In practical engineering applications, the dynamic and vibration characteristics of the bearing

* Corresponding author.
E-mail address: zhouwenjiezwj@ujs.edu.cn (W. Zhou).

https://doi.org/10.1016/j.apacoust.2024.110254
Received 29 April 2024; Received in revised form 19 August 2024; Accepted 21 August 2024
Available online 24 August 2024

Nomenclature

U	strain energy[-]
P_i	action of arbitrary force[-]
g_{ij}^{o}	the uncracked flexibility [-]
g_{ij}^{c}	the additional flexibility of crack [-]
k	the shear shape coefficient
h	the width of the thin plate[mm]
α	the crack depth on the thin plate[mm]
R	the rotor radius[mm]
θ_c	the crack inclination angle[°]
σ	normal stress[MPa]
τ	shearing stress[MPa]
l	the length of the crack element[mm]
$\mathbf{K}^s$	stiffness matrix in the stationary coordinate system [N/mm]
$\mathbf{K}^g$	stiffness matrix in rotating coordinate system [N/mm]
$\mathbf{T}_g$	global transformation matrix
$\mathbf{T}_c$	coordinate transformation matrix
ω	rotation speed [rad/s]
A_{1m}	the axial distance between the loci of inner and outer raceway groove curvature centers[mm]
A_{2m}	the radial displacement between the loci of the groove curvature centers[mm]
δ_a	axial displacement [mm]
δ_r	radial displacement [mm]
θ_b	angular displacement
α^o	the original contact angular[°]
R_i	the radius of the locus of inner race groove curvature centers[mm]
ψ_m	the azimuth of ball m[°]
X_{1m}	the axial projection of the distance between the ball center and the outer race groove curvature center[mm]
X_{2m}	the radial projection of the distance between the ball center and the outer race groove curvature center[mm]
δ_{im}	the inner race contact deformations [mm]
δ_{om}	the outer race contact deformations [mm]
F_a	the axial load [N]
F_r	the radial load [N]
M	the moment [N·mm]
Z	the number of balls
$\psi_{a1,b1}(t)$	the daughter wavelets[-]
b_1	the time parameter[-]

significantly affect the operation of the rotor system. Hou et al. [22] studied the dynamics of transverse cracked Jeffcott rotor with ball bearings. Their research focused on diagnosing the nonlinear dynamic behavior of an aircraft ball bearing-rotor system with a crack under maneuver loads. Vashisht and Peng [23] established a nonlinear system of a cracked rotor with a ball bearing and investigated the influence of this system on crack detection. The results showed that the presence of rolling bearings had a negative impact. Xiang et al. [24,25] developed a multi-fault rotor bearing system considering the effects of cracks, oil-film forces and rub-impact. Their research revealed enriched behavior in the two-stage bearing-rotor system, with the ability to detect crack near the half of subcritical speed. However, there are few reports on the research of cracked rotor-angular contact ball bearing system.

With the continuous advancement and refinement of theoretical models for cracked rotors, numerous methods for diagnosing rotor cracks have been summarized by scholars, relying on these theoretical models and experimental systems. Darpe [26] proposed a novel diagnostic method by applying excitation to different angular directions of cracks and using wavelet transform to capture the transient response in lateral vibration caused by transient torsional excitation. Gasch [27] conducted stability analysis on a Laval rotor with crack and observed that as the crack grew, the amplitudes at 1X, 2X, and 3X increased. Sinou and Lees [28,29] analyzed the evolution of the orbits at various locations of the cracked rotor around 1/2 and 1/3 of the first critical speed. Al-Shudeifat [30] performed critical and subcritical harmonic analysis on a rotor with open transverse cracks, confirming that the whirl orbits with inner loops were unique to breathing cracks. Additionally, wavelet transform has shown excellent performance in processing experimental data. Guo et al. [31] combined Empirical Mode Decomposition (EMD) with wavelet transform spectra to examine the dynamic characteristics of a cracked rotor. The results revealed that the 3X and 2X super-harmonic components exhibited distinct signatures, serving as accurate indicators for early detection of cracks. Subsequently, they conducted an experimental investigation [32], where the appearance of inner loops in whirl orbits proved effective for crack identification in the cracked rotor system when the rotation speed approaches respectively around 1/2, 1/3, 1/4, and 1/5 subcritical speed. Lu et al. [33] employed a Kriging proxy model to identify rotor cracks based on the super-harmonic nonlinear characteristics using an update method. The results showed that two measurement points were highly useful for real-world applications. Compared with the existing research, the cracked rotor model and experimental results given by scholars are a relatively perfect reference. Its vibration signal is very pure, with only rotation frequency and 2X component in frequency domain. However, there may be a large number of redundant signals in the system vibration signals detected in the actual use environment. These redundant signals may be caused by minor defects in other parts of the rotor or the system itself. Therefore, it is very important to eliminate the interference of these redundant signals and observe the vibration signals better.

Regarding the application of Empirical Mode Decomposition (EMD) in rotating machinery, Lei et al. [34] provided a summary. In their review, they mentioned that EMD exhibits end effects and mode mixing issues when dealing with transient signals. These problems greatly affect the judgment of fault signals. To address this issue, subsequent improvement methods have provided some directions. Among them, CEEMDAN has gained wide popularity in fault diagnosis as an improved method that can overcome the drawbacks of EMD. Chen et al. [35] applied CEEMDAN to identify axial unbalance. The signals became easier to recognize after processing with CEEMDAN. Hu et al. [36] used CEEMDAN for vibration signal denoising in their study on brake disc unbalance detection. In Hu's research, the advantages and weaknesses of EMD, EEMD and CEEMDAN are compared in detail. Compared with EEMD and CEEMDAN, EMD has the problem of mode mixing when dealing with relatively complex simulation signals. After the signal reconstruction, the signal processed by CEEMDAN is smoother, which is obviously better than the other two methods.

According to the above researches, the influence of angular contact bearing on the dynamics of cracked rotor system is still less explored. The raceway control theory proposed in J-H model still has high value for angular contact ball bearing [37,38]. It is feasible to calculate the specific parameters of bearing by J-H model and obtain the actual bearing stiffness by combining the stiffness matrix. For breathing crack, the model proposed by Darpe et al. [9] can estimate shaft stiffness and represent breathing effect. This novel model can be adapted to any steady or transient rotation speed and excitations. Therefore, the proposed model can better predict the vibration characteristics of cracked rotor-bearing system compared with the previous model.

In this paper, the theoretical basis is firstly established for a model of double-disk cracked rotor-rolling bearing system. Subsequently, the actual vibration signals are obtained through experiments, and these

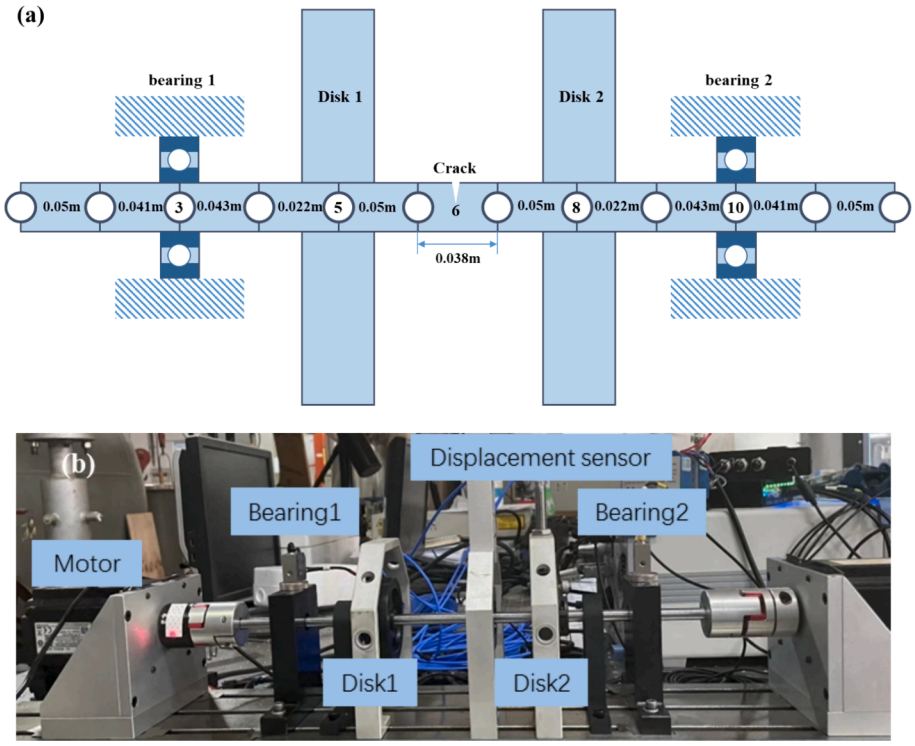

Fig. 1. Double-disk cracked rotor system and experimental system: (a) theoretical model; (b) experimental system.

Table 1
Parameters of double-disk rotor system.

Parameters	Values
Shaft diameter	10 mm
Shaft length	450 mm
Mass of disk	0.49 kg
Density of shaft	7850 kg/m^3
Young's modulus	2.11 × 10^{11}N/m^2
Unbalanced mass	1 g
Bearing	7200C

signals are analyzed by traditional FFT and CWT. Then the CEEMDAN-CWT is used to decompose the signal to remove the interference signal, and its relatively pure time–frequency information is obtained through CWT spectrum. Finally, the theoretical results are compared and analyzed. The study results offer a new idea and method for the complex signal study of multi-stage rotor systems.

2. Mathematical modelling and experimental setup

In this paper, a dynamic model of a 6-DoFs crack rotor system with rolling bearing is proposed. The schematic diagram of rotor-bearing system is presented in Fig. 1. The shaft is discretized into 11 finite elements. There is a disk on node 5 and node 8 respectively. The node 3 and 10 are bearings and a transverse crack is in the element 5. For discretization, Timoshenko beam elements are applied. The displacement and acceleration of the shaft can be observed from the vertical, horizontal and axial directions.

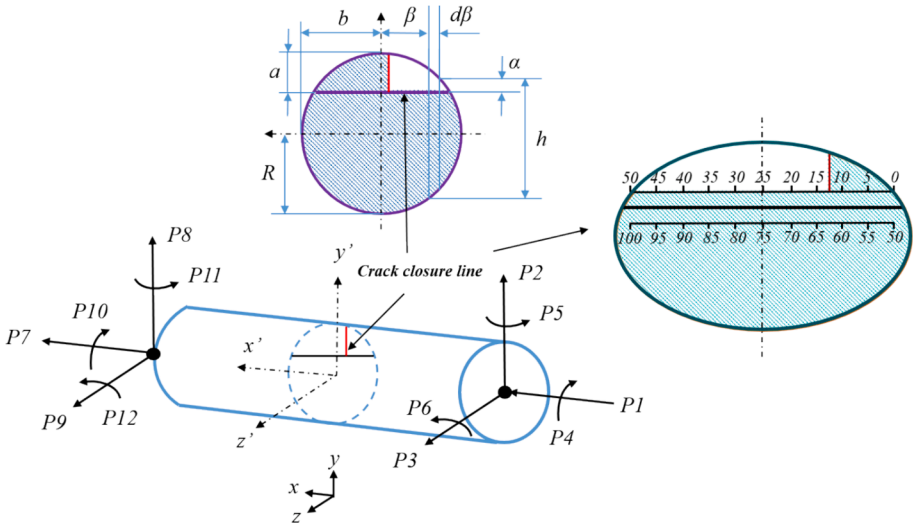

Fig. 2. Cracked shaft loaded with six general forces and cross section of crack with CCL.

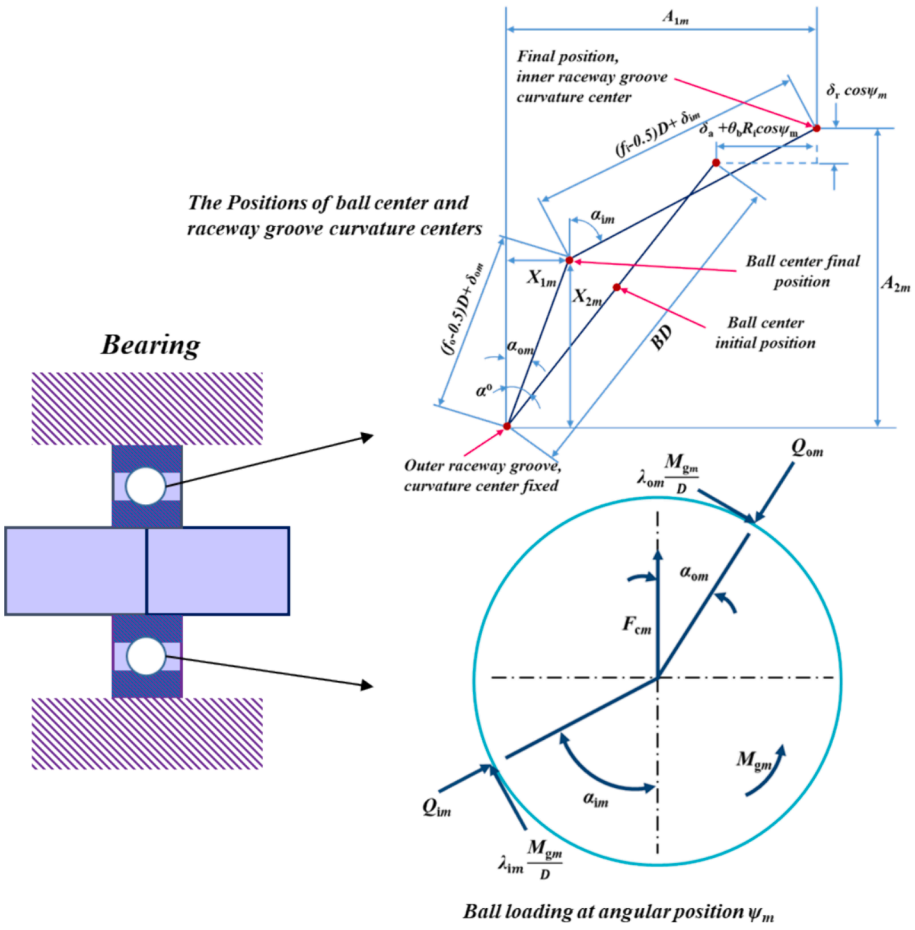

Fig. 3. Geometric and mechanical relationship of rolling bearing.

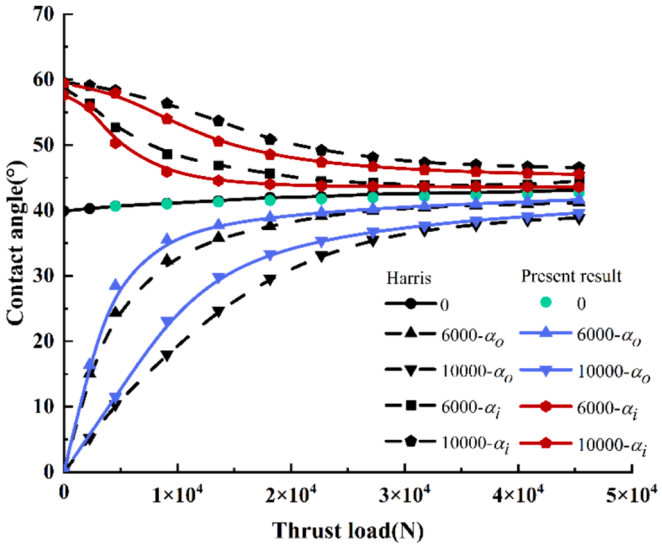

Fig. 4. The verification of bearing model.

2.1. The equations of motion

The equations of motion for a crack rotor system is defined as follows [37,39]:

$$\mathbf{M}_R\ddot{\mathbf{X}} + (\mathbf{C} + \omega\mathbf{D})\dot{\mathbf{X}} + (\mathbf{K} + \mathbf{K}_b)\mathbf{X} = \mathbf{F} \tag{1}$$

where $\ddot{\mathbf{X}}$, $\dot{\mathbf{X}}$ and $\mathbf{X}$ are the generalized acceleration, velocity and displacement of the system, respectively. $\mathbf{M}_R$, $\mathbf{C}$, $\omega\mathbf{D}$ and $\mathbf{K}$ are the mass, damping, gyroscopic and stiffness matrices, respectively. $\mathbf{K}_b$ is the bearing stiffness matrix. $\mathbf{F}$ is the load vector containing the systemic unbalance force, gravity, and external excitations. Values of the parameters are offered in Table 1.

The experimental rotating shaft adopts healthy rotor and cracked rotor with 40 % crack depth (The depth is 4 mm) as test objects. The parameters of the experimental shaft are the same as the simulation (Table 1). The shaft length is 450 mm and the diameter is 10 mm. Sensors for monitoring displacement are installed on the disk 2, and displacement results in vertical and horizontal directions can be obtained. The sampling frequency of the displacement sensor is 8192 Hz, and the sampling time is 4 s. Their vibration signals were collected at 1000 rpm, 2000 rpm and 3000 rpm, respectively. Unbalanced mass is considered on the disk 2.

2.2. Stiffness matrix of crack

According to Castingliano theorem, under the action of arbitrary force P_i, the displacement in its direction can be expressed as [40]:

$$u_i = \frac{\partial U}{\partial P_i} \tag{2}$$

Then the flexibility matrix of the element with the dimension of 12 × 12 can be obtained, the elements in the corresponding position can be expressed as:

$$g_{ij} = \frac{\partial^2 U}{\partial P_i P_j}; i,j = 1 \sim 6 \tag{3}$$

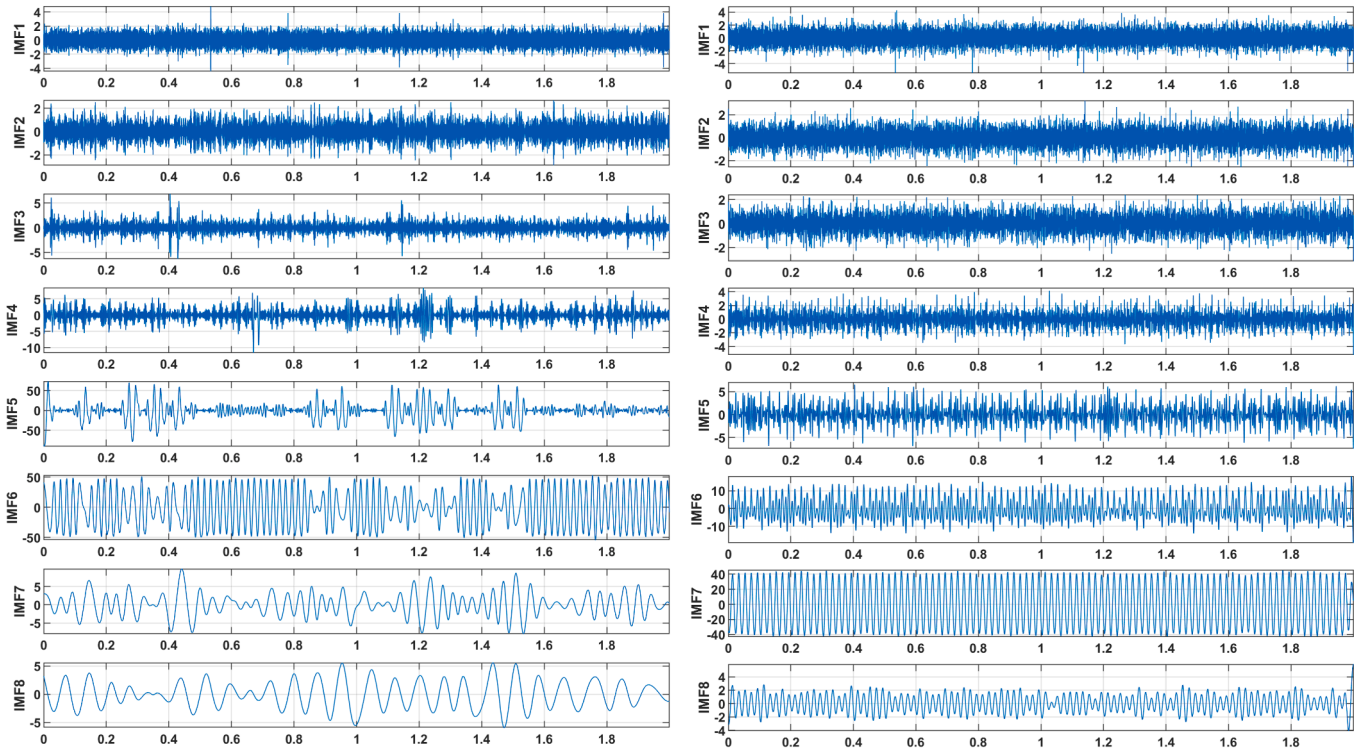

(a) EMD (b) CEEMDAN

Fig. 5. Comparison of results between EMD and CEEMDAN.

Considering the influence of cracks, the total flexibility matrix can be written as the sum of the flexibility matrix of normal shaft section and the additional flexibility matrix caused by cracks:

$$g_{ij} = g_{ij}^{o} + g_{ij}^{c} = \frac{\partial^2 U^{o}}{\partial P_i \partial P_j} + \frac{\partial^2 U^{c}}{\partial P_i \partial P_j} (i,j = 1 \cdots 6) \tag{4}$$

In order to establish the completed system to describe the crack rotor, the cracked shaft is also 6-DoFs. The imaginary line CCL varies continuously during the rotation, which is shown in Fig. 2.

The stress intensity factor is expressed as follows. k can be written as $k = \frac{6(1+\nu)}{7+6\nu}$ for circular sections is given in Ref. [12]. The stress intensity factors (SIF) are given as follows:

$$\begin{cases} K_1^I = \sigma_1^{\theta_c}\sqrt{\pi\alpha}\,F_1(\alpha/h) = \sigma_1 \sin^2\theta_c F_1(\alpha/h) = \dfrac{P_1}{\pi R^2}\sqrt{\pi\alpha}\sin^2\theta_c F_1(\alpha/h) \\ K_2^I = 0 \\ K_3^I = \sigma_3^{\theta_c}\sqrt{\pi\alpha}\,F_1(\alpha/h) = \tau_3 \sin 2\theta_c \sqrt{\pi\alpha}\,F_1(\alpha/h) = \dfrac{kP_3}{\pi R^2}\sqrt{\pi\alpha}\sin 2\theta_c F_1(\alpha/h) \\ K_4^I = \sigma_4^{\theta_c}\sqrt{\pi\alpha}\,F_2(\alpha/h) = \tau_4 \sin 2\theta_c F_2(\alpha/h) = \dfrac{P_4 h}{\pi R^4}\sqrt{\pi\alpha}\sin 2\theta_c F_2(\alpha/h) \\ K_5^I = \sigma_5^{\theta_c}\sqrt{\pi\alpha}\,F_1(\alpha/h) = \dfrac{4(P_5 + P_3(x+\beta\cos\theta_c))\beta}{\pi R^4}\sqrt{\pi\alpha}\sin^3\theta_c F_1(\alpha/h) \\ K_6^I = \dfrac{2(P_2(x+\beta\cos\theta_c) - P_6)h}{\pi R^4}\sqrt{\pi\alpha}\sin^2\theta_c F_2(\alpha/h) \end{cases} \tag{5}$$

According to the above formula, a more complete expression of additional flexibility elements is obtained. Compared with traditional methods, this method is more accurate and quantitative in describing cracks according to the SIF and Castingliano theorem [9].

$$\boldsymbol{G} = \begin{bmatrix} g_{11}^{o} + g_{11}^{c} & g_{12}^{c} & g_{13}^{c} & g_{14}^{c} & g_{15}^{c} & g_{16}^{c} \\ g_{21}^{c} & g_{22}^{0} + g_{22}^{c} & g_{23}^{c} & g_{24}^{c} & g_{25}^{c} & g_{26}^{c} + g_{26}^{o} \\ g_{31}^{c} & g_{32}^{c} & g_{33}^{o} + g_{33}^{c} & g_{34}^{c} & g_{35}^{c} & g_{36}^{c} \\ g_{41}^{c} & g_{42}^{c} & g_{43}^{c} & g_{44}^{o} + g_{44}^{c} & g_{45}^{c} & g_{46}^{c} \\ g_{51}^{c} & g_{52}^{c} & g_{53}^{c} & g_{54}^{c} & g_{55}^{o} + g_{55}^{c} & g_{56}^{c} \\ g_{61}^{c} & g_{62}^{o} + g_{62}^{c} & g_{63}^{c} & g_{64}^{c} & g_{65}^{c} & g_{66}^{o} + g_{66}^{c} \end{bmatrix} \tag{6}$$

The stiffness matrix of crack element is obtained by transfer matrix **T** [41].

$$\boldsymbol{K}^{c} = \boldsymbol{T}\boldsymbol{G}^{-1}\boldsymbol{T}^{\mathrm{T}} \tag{7}$$

$$\boldsymbol{T}^{\mathrm{T}} = \begin{bmatrix} 1 & 0 & 0 & 0 & 0 & 0 & -1 & 0 & 0 & 0 & 0 & 0 \\ 0 & 1 & 0 & 0 & 0 & 0 & 0 & -1 & 0 & 0 & 0 & l \\ 0 & 0 & 1 & 0 & 0 & 0 & 0 & 0 & -1 & 0 & -l & 0 \\ 0 & 0 & 0 & 1 & 0 & 0 & 0 & 0 & 0 & -1 & 0 & 0 \\ 0 & 0 & 0 & 0 & 1 & 0 & 0 & 0 & 0 & 0 & -1 & 0 \\ 0 & 0 & 0 & 0 & 0 & 1 & 0 & 0 & 0 & 0 & 0 & -1 \end{bmatrix} \tag{8}$$

During the rotation of the rotor, the crack closure line position (CCLP) will move to a certain position for each rotation angle of the rotor, therefore, the CCLP will be evenly and slowly opened from 0 to 50, and then slowly closed from 50 to 100. When the stiffness of the corresponding element in the following coordinate system is calculated, the stiffness matrix $\mathbf{K}^{s}$ in the fixed coordinate system can be solved by combining the global transformation matrix $\mathbf{T}_c$ [9]:

$$\boldsymbol{K}^{s} = \boldsymbol{T}_c^{\mathrm{T}}\boldsymbol{K}^{g}\boldsymbol{T}_c \tag{9}$$

The matrix $\mathbf{T}_c$ can be assembled by matrix $\mathbf{T}_e$ and $\mathbf{T}_e$ is given by:

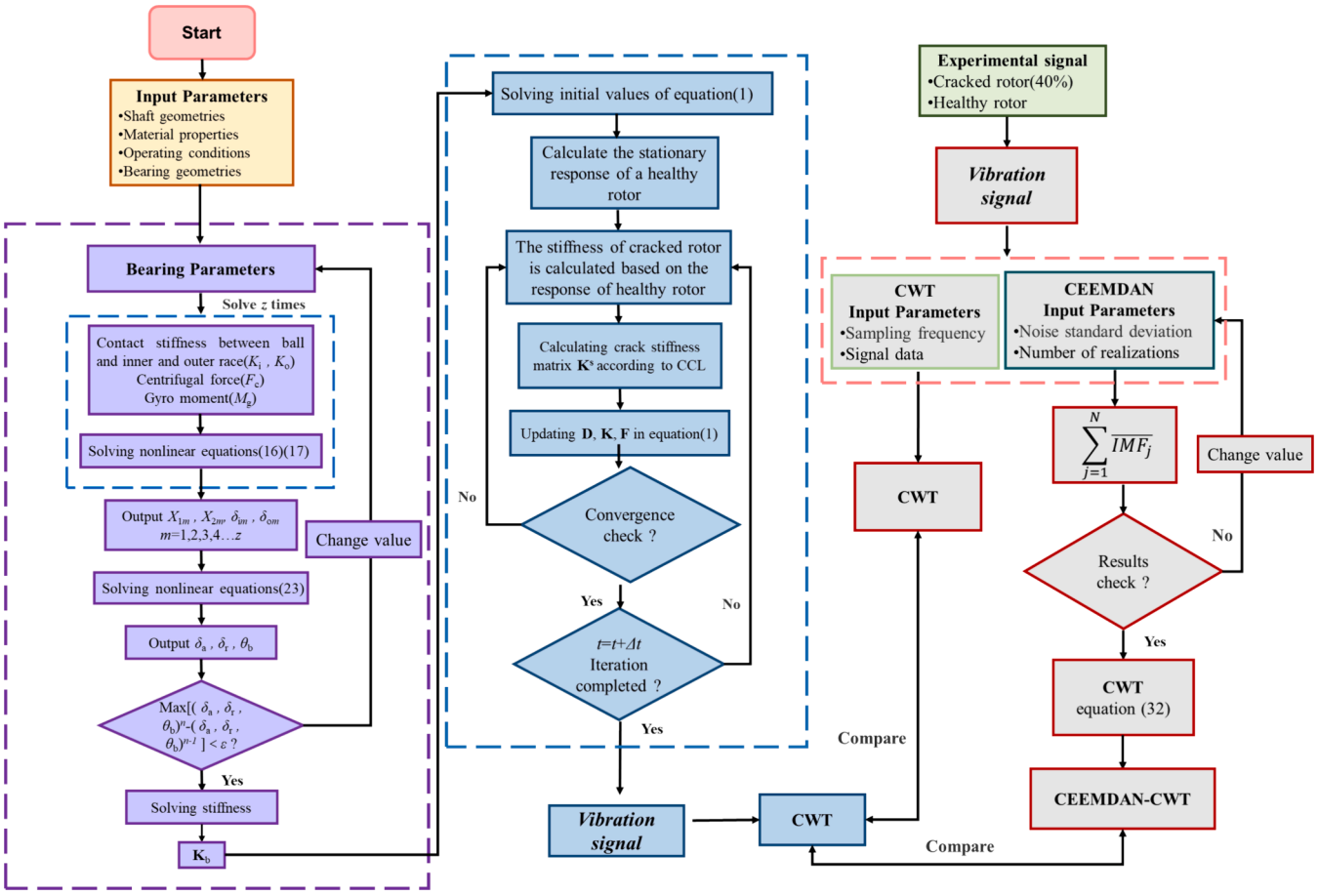

Fig. 6. The flow chart of signal processing.

$$\boldsymbol{T}_e = \begin{bmatrix} 1 & 0 & 0 & 0 & 0 & 0 \\ 0 & \cos\theta_c & \sin\theta_c & 0 & 0 & 0 \\ 0 & -\sin\theta_c & \cos\theta_c & 0 & 0 & 0 \\ 0 & 0 & 0 & 1 & 0 & 0 \\ 0 & 0 & 0 & 0 & \cos\theta_c & \sin\theta_c \\ 0 & 0 & 0 & 0 & -\sin\theta_c & \cos\theta_c \end{bmatrix} \tag{10}$$

2.3. The rolling bearings model

In the research process of mathematical modeling of cracked rotors, bearings are often idealized as fixed support. However, in reality, a rolling bearing is not an ideal support. Its stiffness is related to its own geometric parameters, load, and rotational speed. For the study of rolling bearings, the classic rolling bearings model is established by Jones and Harris [42]. J-H (Jones-Harris) method provides an idea, which considers the centrifugal forces and gyroscopic moments of rolling element. Geometric and mechanical relationship of rolling bearing is shown in Fig. 3. The internal geometric relationship is given as:

$$A_{1m} = BD\sin\alpha^o + \delta_a + \theta_b R_i \cos\psi_m \tag{11}$$

$$A_{2m} = BD\cos\alpha^o + \delta_r \cos\psi_m \tag{12}$$

$$B = f_o + f_i - 1 \tag{13}$$

The relationship between variables on the Fig. 4 is linked by Pythagorean theorem:

$$(A_{1m} - X_{1m})^2 + (A_{2m} - X_{2m})^2 - [(f_i - 0.5)D + \delta_{im}]^2 = 0 \tag{14}$$

$$X_{1m}^2 + X_{2m}^2 - [(f_o - 0.5)D + \delta_{om}]^2 = 0 \tag{15}$$

From Fig. 3, the following equilibrium equation can be obtained by decomposing the load in the horizontal and vertical directions [43]:

$$Q_{im}\sin\alpha_{im} - Q_{om}\sin\alpha_{om} - \frac{M_{gm}}{D}(\lambda_{im}\cos\alpha_{im} - \lambda_{om}\cos\alpha_{om}) = 0 \tag{16}$$

$$Q_{im}\cos\alpha_{im} - Q_{om}\cos\alpha_{om} - \frac{M_{gm}}{D}(\lambda_{im}\sin\alpha_{im} - \lambda_{om}\sin\alpha_{om}) + F_{cm} = 0 \tag{17}$$

Through the conditions of equilibrium of mechanics, the mechanical equations of bearings can be given as:

$$F_a - \sum_{m=1}^{m=Z}\left(Q_{im}\sin\alpha_{im} - \frac{\lambda_{im}M_{gm}}{D}\cos\alpha_{im}\right) = 0 \tag{18}$$

$$F_r - \sum_{m=1}^{m=Z}\left(Q_{im}\cos\alpha_{im} - \frac{\lambda_{im}M_{gm}}{D}\sin\alpha_{im}\right)\cos\psi_m = 0 \tag{19}$$

$$M - \sum_{m=1}^{m=Z}\left[\left(Q_{im}\sin\alpha_{im} - \frac{\lambda_{im}M_{gm}}{D}\cos\alpha_{im}\right)R_i + \frac{\lambda_{im}M_{gm}}{D}r_i\right]\cos\psi_m = 0 \tag{20}$$

$$Q_{om} = K_{om}\delta_{om}^{1.5} \tag{21}$$

$$Q_{im} = K_{im}\delta_{im}^{1.5} \tag{22}$$

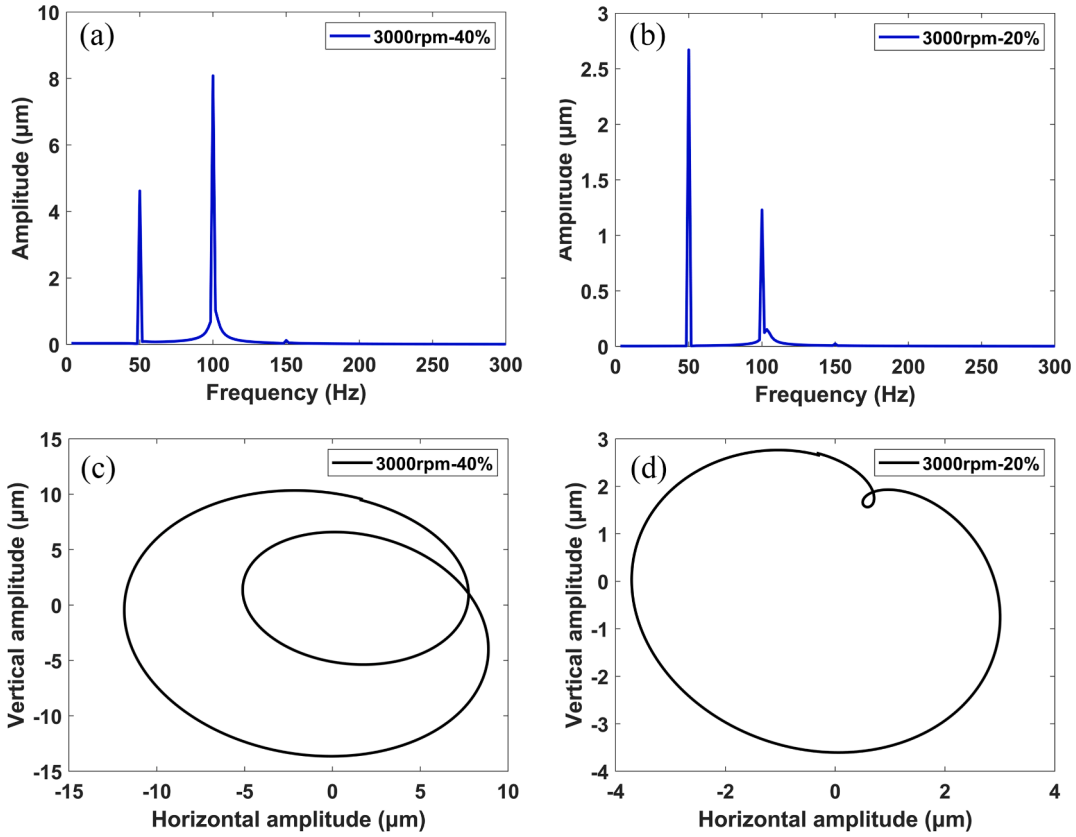

Fig. 7. Simulation results of FFT and whirl orbit: (a) FFT of 40% crack depth; (b) FFT of 20% crack depth; (c) whirl orbit of 40% crack depth; (d) whirl orbit of 20% crack depth.

$$\begin{aligned} F_{\mathrm{a}} - \sum_{m=1}^{m=Z}\left(Q_{im}\sin\alpha_{im} - \frac{\lambda_{im}M_{gm}}{D}\cos\alpha_{im}\right) &= 0 \\ F_{\mathrm{r}} - \sum_{m=1}^{m=Z}\left(Q_{im}\cos\alpha_{im} - \frac{\lambda_{im}M_{gm}}{D}\sin\alpha_{im}\right)\cos\psi_m &= 0 \\ M - \sum_{m=1}^{m=Z}\left[\left(Q_{im}\sin\alpha_{im} - \frac{\lambda_{im}M_{gm}}{D}\cos\alpha_{im}\right)R_{\mathrm{i}} + \frac{\lambda_{im}M_{gm}}{D}r_{\mathrm{i}}\right]\cos\psi_m &= 0 \end{aligned} \tag{23}$$

For the bearing stiffness, a 3 × 3 stiffness matrix is used to represent the support stiffness.

$$\boldsymbol{K}_{\mathrm{b}} = \begin{bmatrix} \dfrac{\partial F_{\mathrm{a}}}{\partial \delta_{\mathrm{a}}} & & \\ & \dfrac{\partial F_{\mathrm{r}}}{\partial \delta_{\mathrm{r}}} & \\ & & \dfrac{\partial M}{\partial \theta_{\mathrm{b}}} \end{bmatrix} \tag{24}$$

According to the quasi-static model of rolling ball bearing established in the previous section, the corresponding calculation program is compiled. The change of contact angle with axial load was selected at the speeds of $n = 0$r/min, 6000r/min and 10000r/min, respectively. The calculated results are compared with the literature's results, which are shown in the Fig. 4.

Through the results of literature and verification, the contact angle tends to be stable with the increased load and the contact angle will increase with the increased speed. These factors affect the actual stiffness of bearings. Considering the main load of the rotor system in this paper comes from the rotor system itself, and the smaller design size brings light load. Therefore, the simulation results have an accurate description in the light load area, which can provide sufficient calculation accuracy for the rotor-bearing system.

2.4. Theoretical description of CEEMDAN

CEEMDAN is an improved method proposed by Torres [44]. A noise is used for each stage of the decomposition, which shows a better separation and a lesser number of sifting iterations. Therefore, based on the complexity of the experimental signal, this method is adopted to decompose the experimental signal and extract the vibration signal of the rotor itself. The decomposition principle of CEEMDAN is as follows [45]:

Define $Uj(\cdot)$ as the operator that produces the j-th mode obtained by EMD, and $N_i(t)$ is the white noise. $h(t)$ is the target signal.

(1) EMD is used to decompose each $h_i(t) = h(t) + \varepsilon_0 N_i(t)$, ($i = 1, \ldots, I,$). The first CEEMDAN mode and the first residue can be expressed as:

$$\overline{H_1} = \frac{1}{I}\sum_{i=1}^{I} H_{i1} \tag{25}$$

$$R_1(t) = h(t) - \overline{H_1} \tag{26}$$

(2) Same method is used to decompose each $R_1(t) + \varepsilon_1 U_1(N_i(t))$, ($i = 1, \ldots, I,$). The second CEEMDAN mode can be expressed as:

$$\overline{H_2} = \frac{1}{I}\sum_{i=1}^{I} U_1(R_1(t) + \varepsilon_1 U_1(N_i(t)))) \tag{27}$$

(3) The j-th, ($j = 2, 3, \ldots, N$) residue is calculated. The ($j + 1$)-th CEEMDAN mode can be defined as:

$$R_j(t) = R_{j-1}(t) - \overline{H_j} \tag{28}$$

$$\overline{H_{j+1}} = \frac{1}{I}\sum_{i=1}^{I} U_1\left(R_j(t) + \varepsilon_j U_j(N_i(t))\right)) \tag{29}$$

Repeat step 3 until the residue cannot be decomposed by EMD.

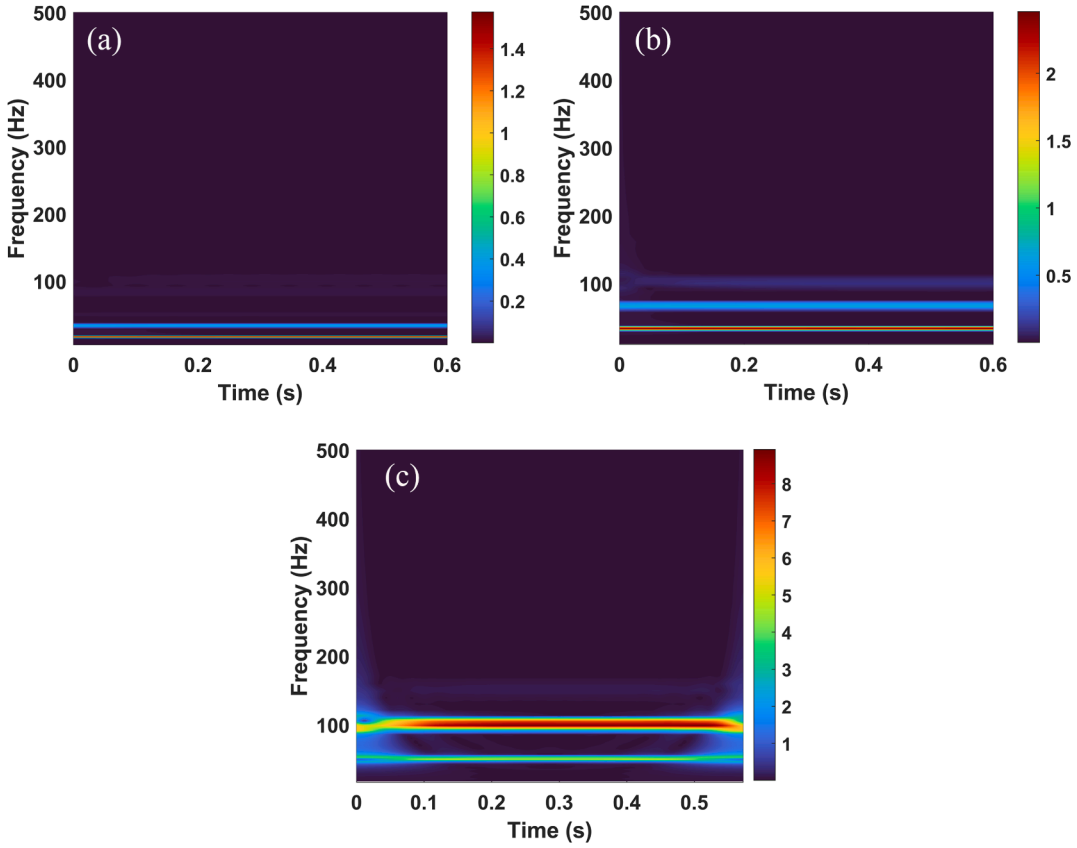

Fig. 8. The theoretical horizontal displacements of cracked rotor-bearing system and CWT for three different rotating speeds: (a) 1000 rpm, (b) 2000 rpm and (c) 3000 rpm.

Therefore, the target signal can be expressed as:

$$h(t) = \sum_{j=1}^{N} \overline{H_j} + R_N(t) \tag{30}$$

The coefficient ε allows the selection of the SNR at each stage. According to Ref. [46], It is pointed out that input SNR has no influence on the performance of CEEMAN, and the recommended values are 0.2. Therefore, values of the added noise of CEEMDAN are set between 0 and 1. According to the EMD and CEEMDAN decomposition of the same experimental signal in Fig. 5, it can be seen that EMD has a mode mixing problem in processing this kind of experimental signal. CEEMDAN 's results are excellent. Every IMF has almost no mode mixing problem, and the unique vibration characteristics can be clearly observed. This is because the adjustable noise is added to cover up the possible interference, which makes the processed signal closer to the ideal signal of EMD, that is, the number of extreme points and the number of zero crossings are equal or not more than one difference in the whole data. However, the average value of the upper envelope formed by the local maximum point and the lower envelope formed by the local minimum point is zero at any moment. This shows that CEEMDAN can effectively process such signals.

Fig. 6 shows the concrete steps of the whole process including CEEMDAN for the signal processing. Initially, in the simulation part, the geometric parameters and operational conditions of the rotor and bearings are incorporated to derive the bearing stiffness and vibration signal of the crack-free rotor. Subsequently, the solution results of the crack-free rotor serve as a foundation for resolving the cracked rotor, leading to further solutions and the ultimate vibration signal.

In the experimental part, the sensor is applied to measure the vibration signal of the cracked rotor under corresponding conditions. The collected signal is then subjected to CWT and CEEMDAN for processing. A comparison is made between the CWT spectra of the simulated and experimental results to identify differences. Following the application of CEEMDAN processing to the experimental signal, a comparison is made with the simulated vibration signal. Results that exhibit similarity to the simulated signal are further subjected to CWT processing to observe their time–frequency characteristics and compare them with the simulated results. The method of combining CEEMDAN and CWT is called CEEMDAN-CWT method, which is used to decompose complex vibration signals and express the decomposed signals through time–frequency information.

3. Results and discussion

3.1. Time domain vibration signal and CWT

In the operation of a double-disk rotor system, observing the rotation frequency and amplitude changes of other frequency components is the key to judge whether cracks appear in the system [25,47]. Fast Fourier transform (FFT), as a traditional method to process time domain signals, is widely used in the calculation of frequency spectrum. But this method can't display the instantaneous frequency. Sinou [48] describes a method of analyzing cracked shaft using continuous wavelet, in which can be defined as:

$$W(a_1, b_1) = \int_{-\infty}^{+\infty} f(t)\psi^*_{a_1,b_1}(t)\mathrm{d}t \tag{31}$$

$$\psi_{a_1,b_1}(t) = \frac{1}{\sqrt{a_1}}\psi\left(\frac{t-b_1}{a_1}\right) \tag{32}$$

Continuous wavelet spectrum describes the frequency intensity of a signal on the time scale. Therefore, the frequency changes of the system

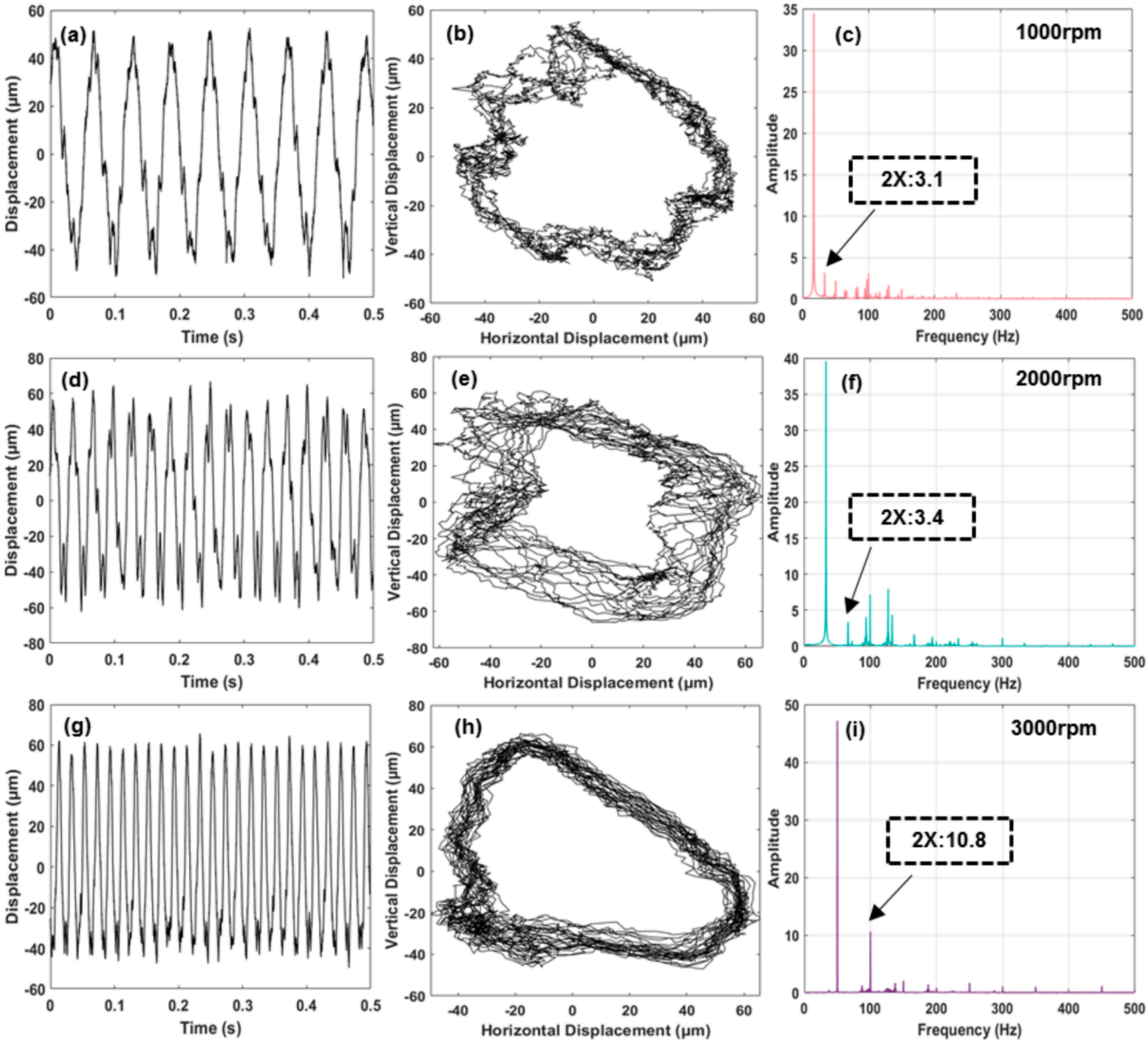

Fig. 9. Dynamics of cracked rotor systems with unbalanced mass: (a) time domain – 1000 rpm, (b) whirl orbit – 1000 rpm, (c) FFT – 2000 rpm, (d) time domain – 2000 rpm, (e) whirl orbit – 2000 rpm, (f) FFT – 2000 rpm, (g) time domain – 3000 rpm, (h) whirl orbit – 3000 rpm, (i) FFT – 3000 rpm.

at different time nodes can be observed during its operation. It is more valuable in time scale than FFT spectrum.

3.1.1. *The theoretical results and CWT*

The time domain signal of cracked rotor contains abundant vibration information, it can be further processed to obtain frequency spectrum and whirl orbit of rotor system for fault analysis. The theoretical time domain vibration signal of cracked rotor-bearing system with double-disk is solved. In addition, the realistic experimental rotor vibration signals are also obtained to further signal processing.

The stiffness of bearing seat is also considered due to the actual rotor system structure. Fig. 7 shows the response results of the theoretical model constructed in this paper at 3000 rpm with different crack depths. From Fig. 7(a) and Fig. 7(b), it can be found that the change of crack depth affects the amplitude change of each frequency component, and the deeper the depth, the greater the amplitude. For the whirl orbit, it can be seen in Fig. 7(c) and Fig. 7(d) that the whirl orbit with inner loops can be clearly observed considering the breathing crack model in section 2.

Fig. 8 shows the theoretical corresponding CWT for three different speeds when the disk 2 has an unbalanced force. With the increased speed, the amplitude increases. The rotation frequency and 2X frequency can be captured through CWT. These frequencies show a banded distribution in time, which is similar to the results of Refs. [30] and [31]. The amplitudes of rotation frequency and 2X frequency also increase with the increased speed.

3.1.2. *The experimental results and CWT*

However, the experimental rotor vibration signals are obviously more complex than the theoretical signals, which are revealed in Fig. 9. With the increased speed, the amplitude of time domain signal increases, and the time domain signals are not stable at different speeds. The result of Fig. 9(e) is similar to those in Ref. [13], but the inner ring is not easy to be observed. When the speed increases to 3000 rpm, the orbit of the system is similar to an oblate circle. The FFT spectrums of cracked rotor at three speeds are also observed, which shows that the rotation frequency increases with increased speed. The frequencies of 3X and 4X are obvious at 2000 rpm, and the 2X frequency is higher than the former at

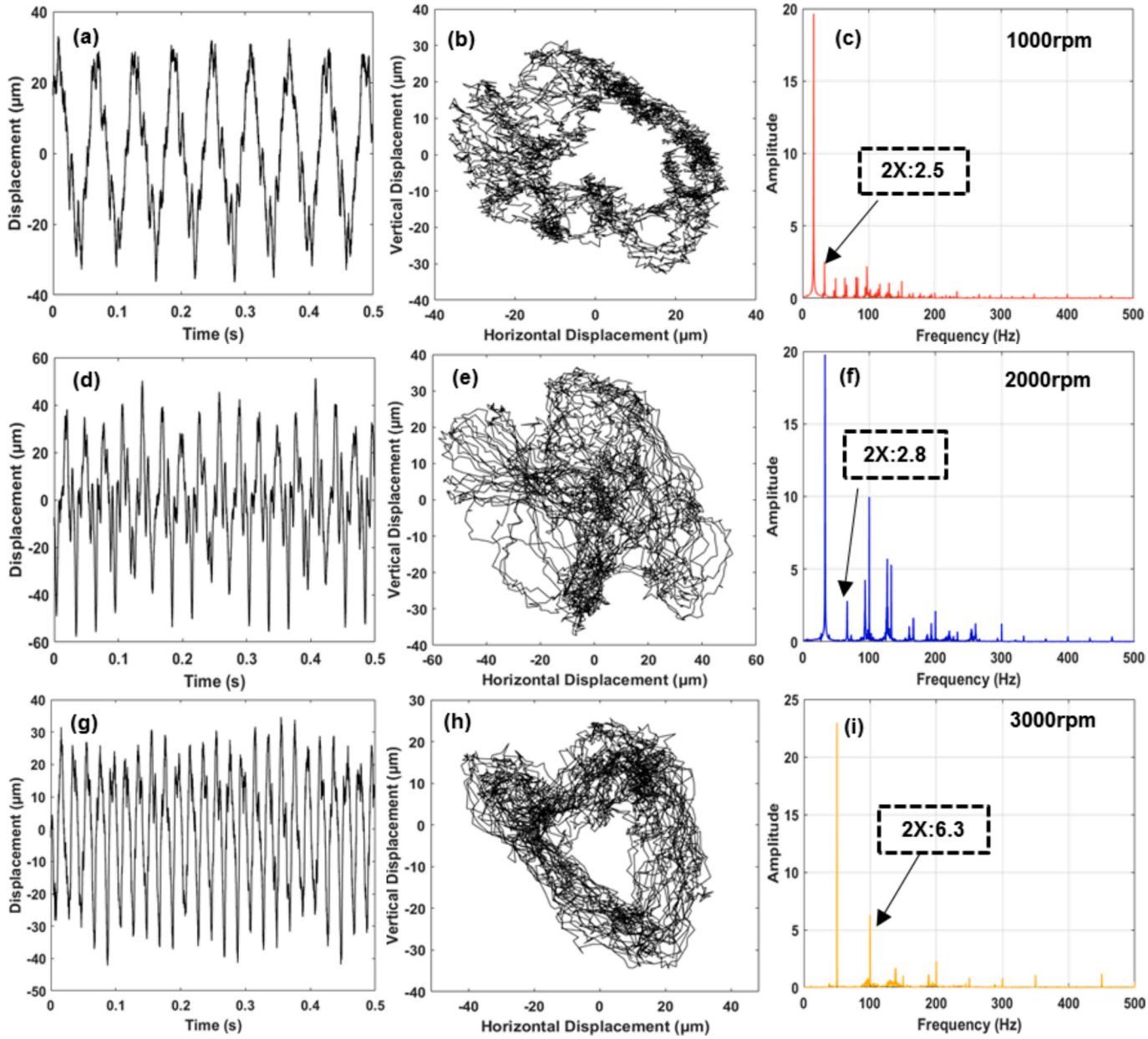

Fig. 10. Dynamics of healthy rotor systems with unbalanced mass: (a) time domain – 1000 rpm, (b) whirl orbit – 1000 rpm, (c) FFT – 2000 rpm, (d) time domain – 2000 rpm, (e) whirl orbit – 2000 rpm, (f) FFT – 2000 rpm, (g) time domain – 3000 rpm, (h) whirl orbit – 3000 rpm, (i) FFT – 3000 rpm.

3000 rpm. According to the results in Ref. [32], the whirl orbits of 1/3 critical speed in the reference is similar to the results in Fig. 9(e), but the results of 1/2 critical speed are different from those in Fig. 9(i). The breathing crack identification method can't be applied well from the regular whirl orbit and frequency spectrum.

Fig. 10 shows the vibration signal of a healthy rotor. With the increased speed, the time domain amplitude increases continuously. The orbits ring of a healthy rotor system is smaller than that of a cracked rotor system, but it is not a relatively obvious circle like the orbits of an ideal healthy rotor. The 2X, 3X and 4X frequencies also exist in the FFT spectrums. Comparing the FFT spectra of Fig. 9 and Fig. 10, it can be observed that the 2X frequency of cracked rotor is slightly higher than that of healthy rotor, and this phenomenon is more obvious with the increased speed. This phenomenon is similar with the results of Ref. [49]. This is because FFT can't display the complete information on time scale, it is necessary to put the experimental signal into CWT spectrum to observe the vibration characteristics of the actual rotor system.

The CWT spectrums from Fig. 11 show the experimental results at different rotation speeds. Not only the rotation frequency but also other frequency components can be observed in the experimental signals. From CWT spectrum, the vibration frequency of rotor system can be displayed on time scale. The frequency distribution proposed by FFT and the time variation characteristics of each frequency intensity both can be observed. For the rotation frequency, there is a stable band distribution at three rotating speeds, which is also mentioned in Ref. [30]. However, the fluctuations phenomena of 3X and 4X frequencies can be clearly caught in Fig. 11(c) and Fig. 11(d) at 2000 rpm. For this kind of fluctuation, it seems to imply the vibration impact of the rotor system.

Compared with the theoretical CWT spectrums and the results which are mentioned in Ref. [30] and [31], it can be observed that there are not huge amplitude 3X and 4X frequencies when the rotating speed is 2000 rpm. The results show that neither open crack nor breathing crack can make the system appear such fluctuations on the time–frequency

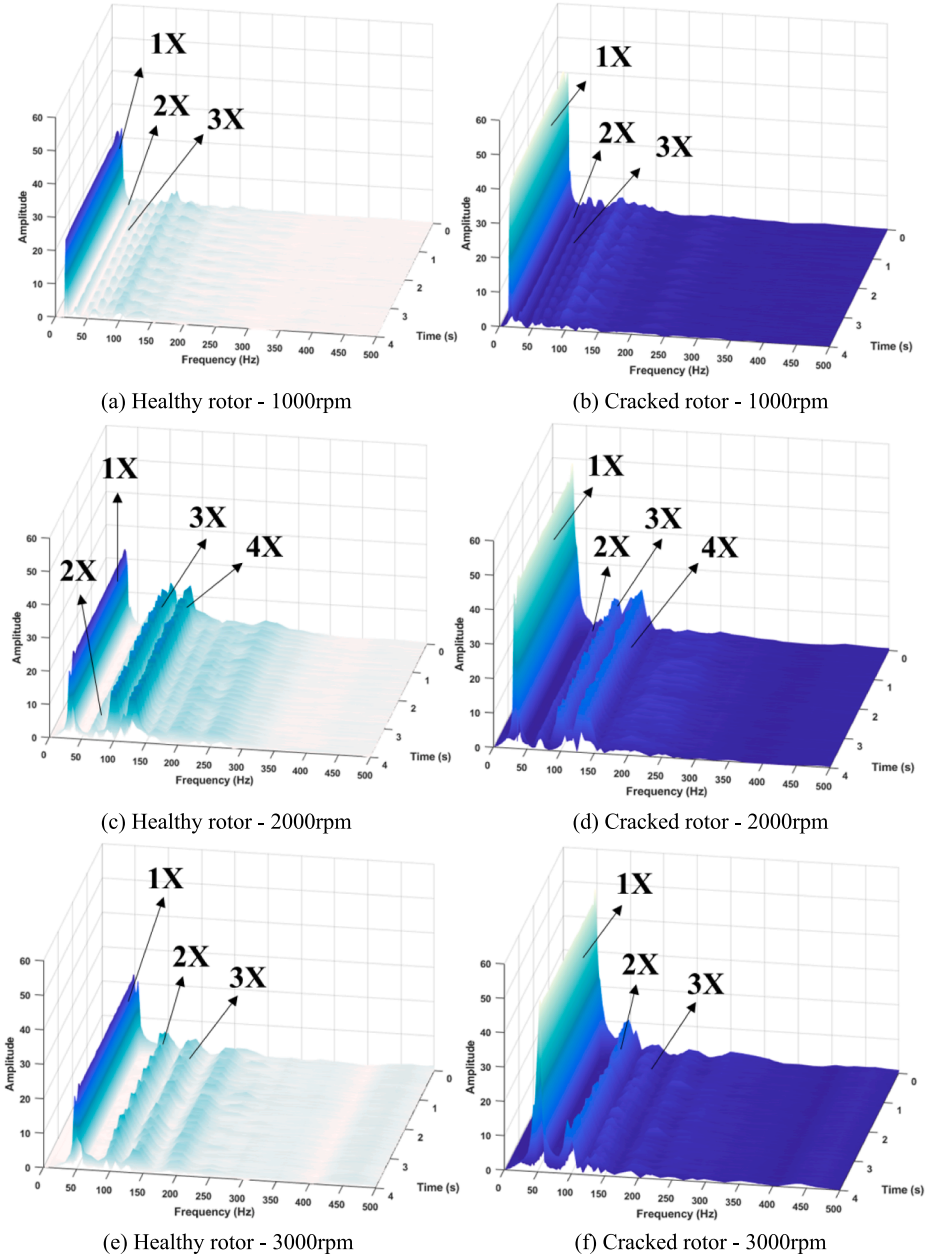

(a) Healthy rotor - 1000rpm (b) Cracked rotor - 1000rpm

(c) Healthy rotor - 2000rpm (d) Cracked rotor - 2000rpm

(e) Healthy rotor - 3000rpm (f) Cracked rotor - 3000rpm

Fig. 11. Experimental horizontal displacement (disk 2 with unbalanced mass) and CWT for healthy rotor and cracked rotor with and three speed: (a–b) 1000 rpm, (c–d) 2000 rpm, (e–f) 3000 rpm.

diagram at a stable speed. In Fig. 8, no similar fluctuation can be observed. For a rotor system, bearings and couplings are also involved in the operation in addition to the shaft part. If these components are misaligned during installation, their vibration frequency may be excited. Therefore, this phenomenon seems to imply that these frequencies are not caused by cracks. These unavoidable influencing factors increase the recognition accuracy and difficulty of the fault recognition for crack rotor-bearing system. Therefore, it is necessary to extract the vibration signal of the rotor itself for better observation.

3.2. Signal analysis by the coupled CEEMDAN-CWT method

The above-mentioned issues are addressed in this section by utilizing CEEMDAN to decompose these signals and extract the characteristic signals of the rotor itself. Subsequently, the accuracy of the decomposition is verified through time–frequency analysis using the CWT spectrogram.

Based on the CEEMDAN method, many IMF components are obtained through decomposition. The first to eighth components are selected as the main analysis targets. As Fig. 12 shows, the experimental signal has many forms, but the most important signal form appears in IMF7 or IMF8. It can be seen that the main signal presents a sine-like wave, which is similar to the waveform observed by simulation. Compared with the components of healthy rotor system, the existence of cracks for cracked rotor system will affect the amplitude of IMF7 (1000 rpm) and IMF8 (2000 rpm, 3000 rpm), but the amplitude of other components has little change. According to the above analysis, it is inferred that this is a vibration signal belonging to the rotor system itself.

Small amplitude vibration signal appears in the signals of healthy and cracked rotor system at various speeds, and their amplitude ranges are very close, which implies that this vibration component is not affected by other factors. It is speculated that the test platform is placed on another flat platform, and the vibration of the test platform itself is excited during the operation of the rotor, which affects the sensor's

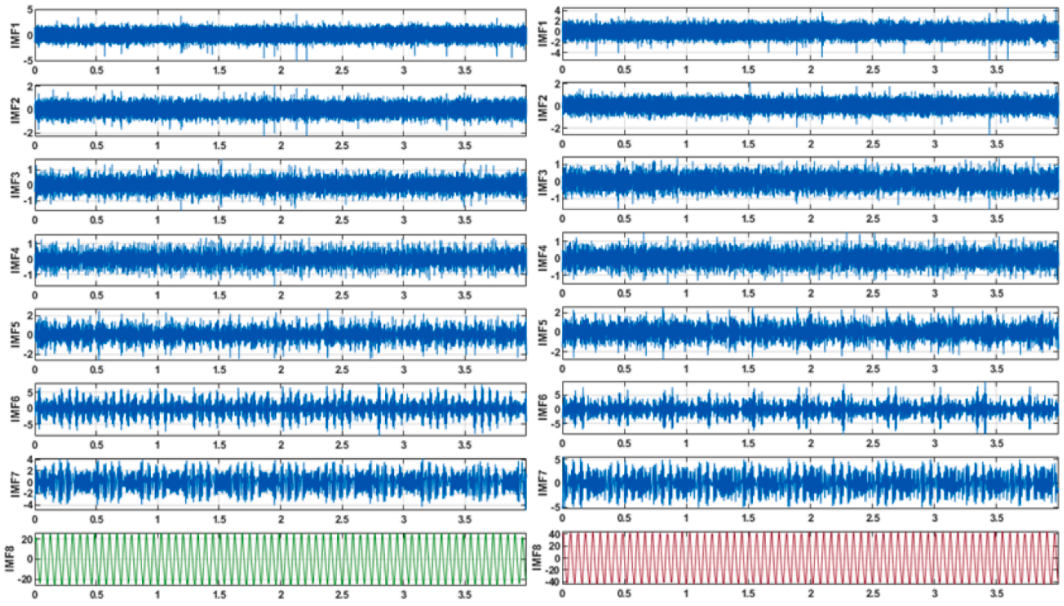

(a) healthy rotor - 1000rpm (b) cracked rotor - 1000rpm

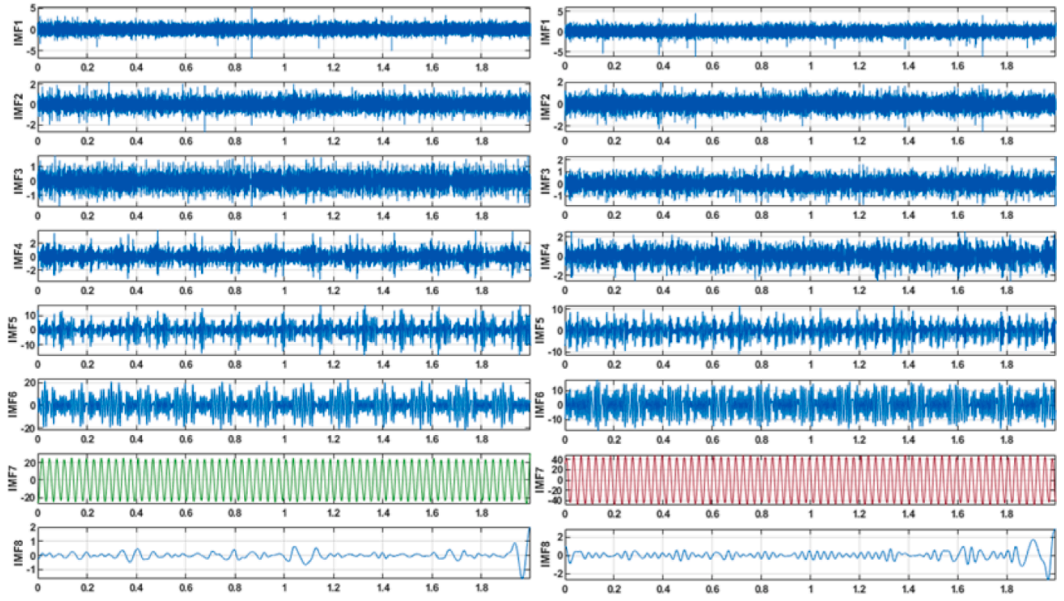

(c) healthy rotor - 2000rpm (d) cracked rotor - 2000rpm

Fig. 12. IMF components obtained by CEEMDAN decomposition of experimental time domain signals of cracked rotor and healthy rotor with unbalanced mass.

monitoring of the vibration of the rotor itself. For the 5th to 6th component (2000 rpm – 3000 rpm) or the 7th component (1000 rpm), the obvious periodic fluctuation can be observed. This fluctuation varies in amplitude at different speeds, which is related to rolling bearings or other rotating parts. The original signals can be decomposed one by one, and the amplitude and vibration characteristics of various vibration signals can be observed more completely through CEEMDAN.

From the results of CEEMDAN, it can be observed that the experimental signal contains rich dynamic characteristics. If these dynamic characteristics are only analyzed by FFT, their changes in time scale will be covered up because of FFT's own characteristics. Therefore, CWT can better explore the reasons for the differences between experiments and simulations from the time–frequency perspective.

In Fig. 13, it can be observed that the frequency distribution from the first to the sixth components moves from the high frequency band to the low frequency band. It can be observed that each IMF component has a fixed distribution in specific frequency bands. As the IMF number increases, these distributions become more concentrated and clearer, with little presence of other information in other frequency bands. This indicates that CEEMDAN successfully separates these complex signals step by step in the decomposition process. It proves that CEEMDAN has good performance. The first component is weak in the observation range while the second component is distributed in the high frequency area near 1000 Hz. The appearance of these high-frequency components further confirms that these vibration signals belong to the system itself. Because the rotating part itself has its own natural frequency and it is impossible to appear in such a high frequency band. For the third to fourth components, the frequency is distributed in the middle of the observable range, and with the increased speed, the frequency presents a band distribution, mainly between 300 Hz and 450 Hz. For cracked rotor

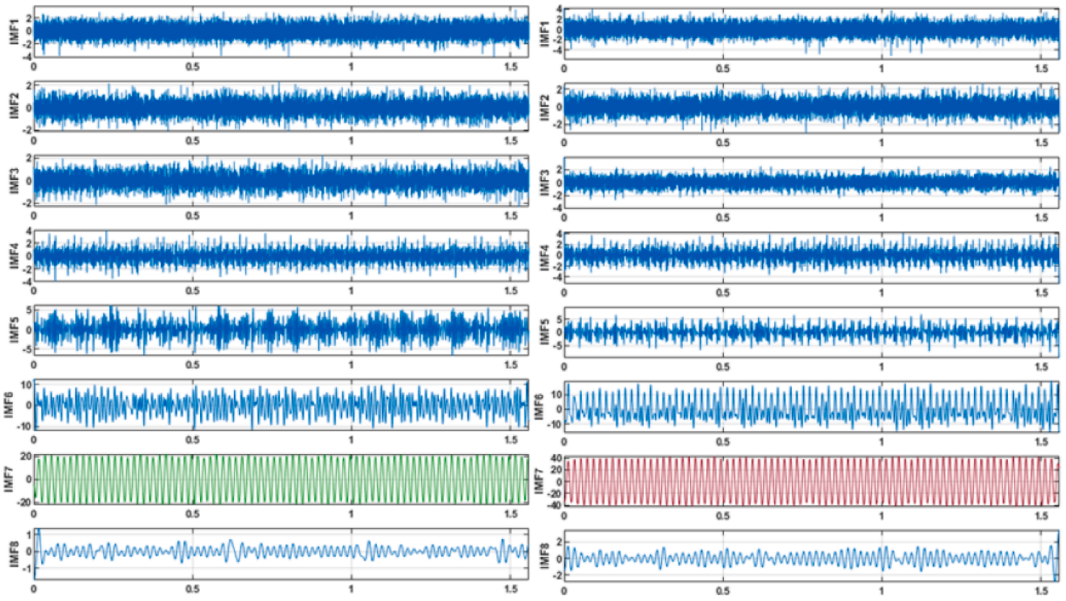

(e) healthy rotor - 3000rpm (f) cracked rotor - 3000rpm

Fig. 12. (*continued*).

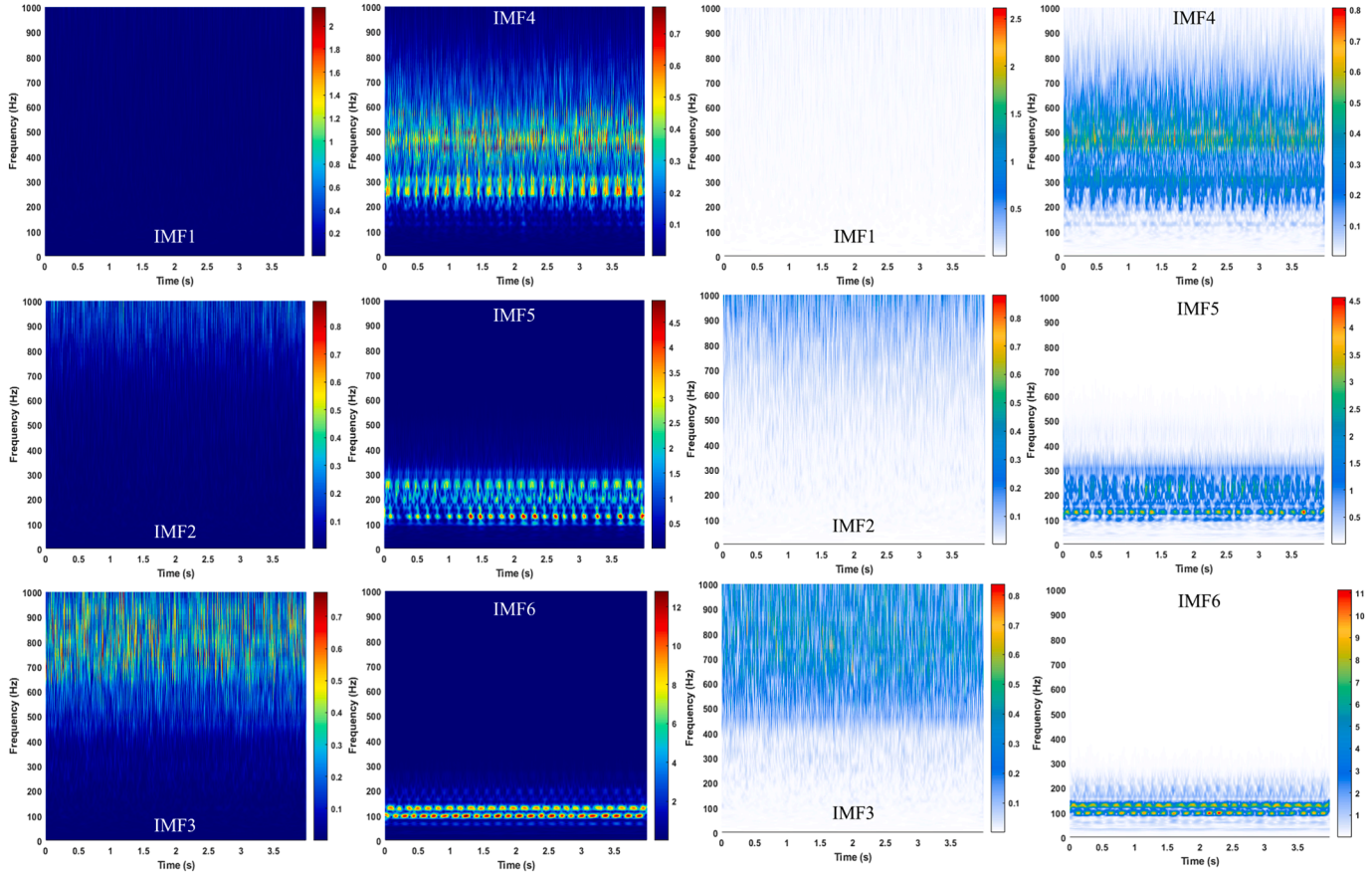

Fig. 13. CEEMDAN-CWT spectrums of cracked and healthy rotor systems with unbalanced mass at 2000 rpm (Blue background-healthy rotor; White background-cracked rotor).

system, a certain distribution can be found in the frequency band below 200 Hz. For the 5th and 6th components at 2000 rpm and 3000 rpm, a large number of intermediate and low frequency signals can be observed, which are mainly distributed between 100 Hz and 400 Hz. In addition, there are a lot of cluster fluctuations in the 5th and 6th components from the CEEMDAN-CWT spectra at different speeds. This phenomenon is very obvious at 2000 rpm as shown in the Fig. 13. The 3X and 4X frequency fluctuation signals are very similar to the 3X and 4X

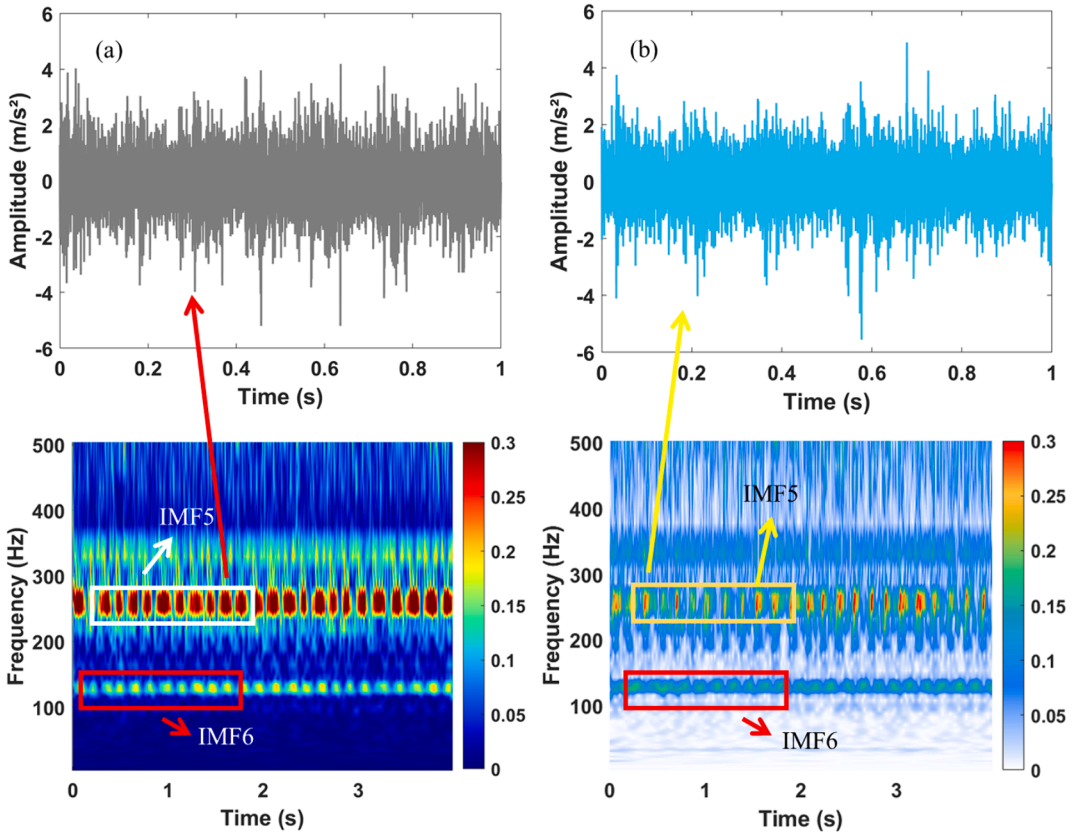

Fig. 14. CWT spectrums of bearing acceleration signal at 2000 rpm: (a) healthy rotor system; (b) cracked rotor system.

frequency fluctuation signals in Fig. 11(c) and Fig. 11(d).

Because the multi-component vibration will be transmitted to each other in the actual system, it is necessary to further explore the influence of bearing vibration on the rotor system. Fig. 14 shows the experimental results of bearing acceleration signals in a healthy rotor system and a cracked rotor system. It can be observed from the time-domain vibration signals that there are certain pulse signals in the running process of bearings, whether it is a cracked rotor system or a healthy rotor system, and these signals are also shown in the CWT spectrum. Through CWT spectrum, it can be observed that the fluctuations similar to those in IMF5 and IMF6 in Fig. 13. This shows that the vibration characteristics of bearings aggravate the complexity of system signals. CEEMDAN-CWT can well separate the bearing vibration signal from the original signal.

When the speed is 3000 rpm (Fig. 15), the amplitudes of these fluctuations are far less than that at 2000 rpm, but they can still be caught. Through a single FFT or CWT processing, it can be observed that numerous frequency information is mixed together, making it difficult to distinguish the causes of the excitation of high frequency components other than the rotational frequency. However, through CEEMDAN-CWT processing, various dynamic information in the rotor vibration signal is reflected in the individual spectrograms, which cannot be obtained by traditional spectrograms. Furthermore, the time–frequency information can be used to further analyze the vibration sources indicated by different IMF components.

Fig. 16 shows the CEEMDAN-CWT spectra of IMF7 and IMF8. The time–frequency information of the experiment is mainly concentrated in the rotation frequency, and the 2X and 3X frequencies of the time-domain signal are very close to the theoretical signals (as shown in Fig. 8) after CEEMDAN-CWT processing. At 1000 rpm and 2000 rpm, a certain 3X frequency component can be observed in both experiment and simulation. Besides, the 3X frequency component is very weak at 3000 rpm. These results shows that the accuracy of the theoretical model has been improved based on the Castingliano theorem and J-H model, which are in good agreement with the experimental results.

In order to better show the amplitude of each frequency, the two-dimensional spectrogram is converted into a three-dimensional spectrogram in Fig. 17. It can be observed from the 3D diagram that the 2X frequency amplitude of a healthy rotor is basically around 3, and its frequency changes little with the change of rotating speed and there is almost no obvious increase. But compared with cracked rotor, its amplitude is about 4 at 1000 rpm. At 2000 rpm, its amplitude exceeds 4, and its maximum value is about 4.4. When the rotating speed changes to 3000 rpm, its maximum amplitude reaches 5. Because the rotating shaft with cracks will increase with the increased rotation speed, and its 2X frequency will obviously increase, it can be seen that these high frequencies of a healthy rotor are probably not caused by cracks. In addition, at the rotating speed below 2000 rpm, the 2X frequency difference between cracked rotor and healthy rotor in CEEMDAN-CWT spectrum is about 1, while the difference of FFT spectrum of original signal is about 0.6, which shows that CEEMDAN-CWT can better judge the difference between the two rotor systems.

Besides, it can be found that there is still a difference in amplitude between the theoretical results and the simulation results. The main reason for the results is that the crack in the experimental rotor is not an ideal crack, which has a great weakening effect on overall stiffness of the rotor system. Compared with the simulation results, it can be seen that the CEEMDAN- CWT method can separate the rotor vibration signal from the complex experimental vibration signal, and the time–frequency spectrum close to the simulation results is observed through CEEMDAN-CWT spectrum. This shows that CEEMDAN-CWT method can better analyze the time–frequency variation characteristics of the rotor system itself.

4. Conclusion

In this paper, the CEEMDAN and CWT are applied to a dual-disk

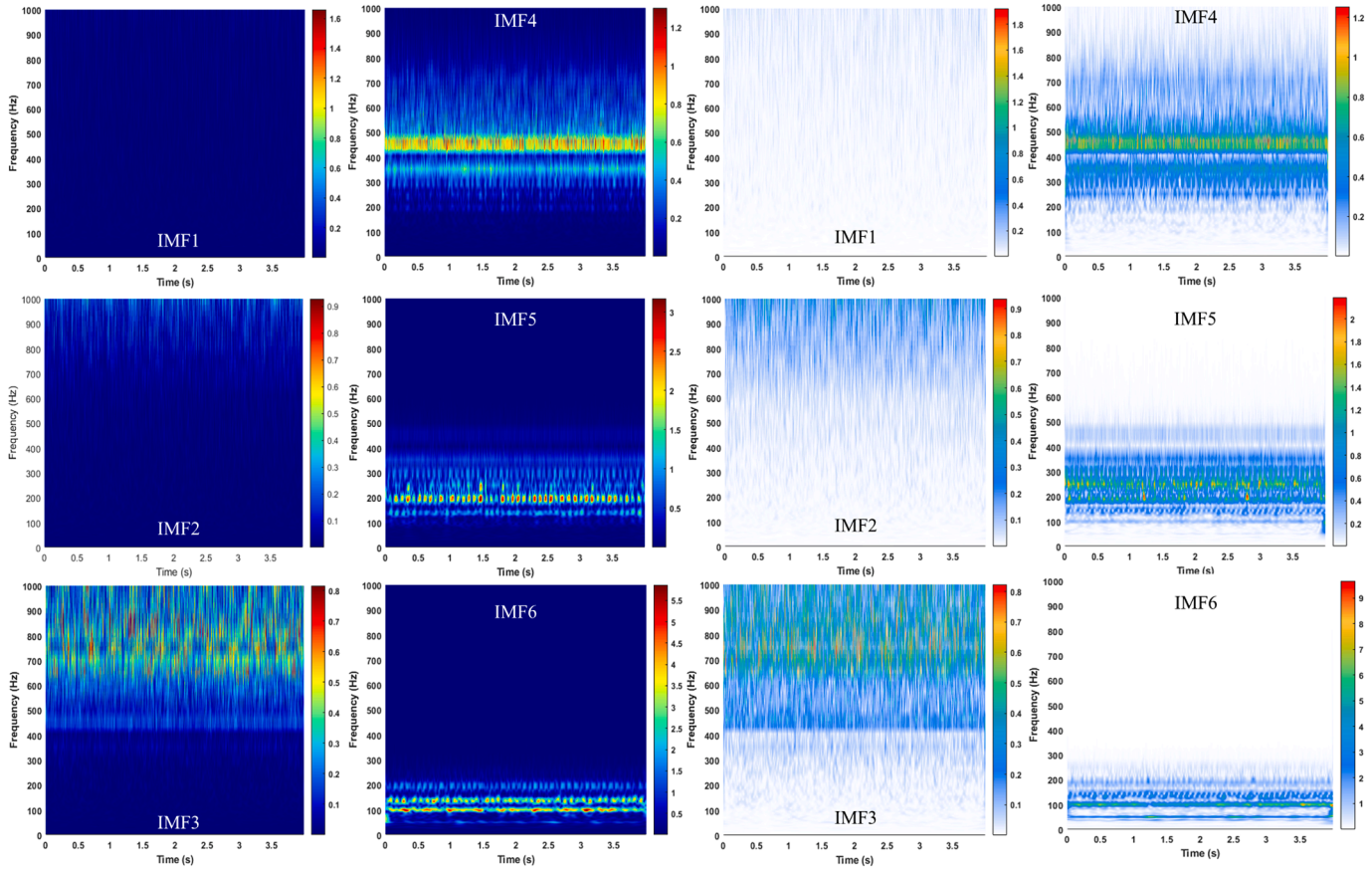

Fig. 15. CEEMDAN-CWT spectrums of cracked and healthy rotor systems with unbalanced mass at 3000 rpm (Blue background-healthy rotor; White background-cracked rotor).

cracked rotor-rolling bearing system to address the challenge of determining the presence of crack faults in cases where complex vibration signals are present in two or even multiple stages of rotor-rolling bearing systems. The vibration signal of double-disk cracked rotor-angular contact ball bearing system is simulated and experimentally explored. The time domain signals of healthy rotor and crack rotor are analyzed by the CEEMDAN and CWT. The calculated results imply that the novel CEEMDAN-CWT method can decompose the complex vibration signal effectively and accurately. The main findings are as follows.

1. Traditional signal analysis methods such as FFT and CWT have shown good performance in processing ideal vibration signals of cracked rotors. However, in practical scenarios, the environment in which the rotor operates makes its vibration signal more complex. When frequency components appear in healthy rotors that are beyond the rotational frequency, these components can interfere with the determination of whether the rotor system has crack faults.
2. CEEMDAN is better than EMD in processing the experimental rotor system signal. There are a large number of signals with similar amplitude and vibration pattern in the experimental signal decomposition results of healthy rotor and cracked rotor, which are not caused by cracks. The results show that the complex experimental rotor vibration signal decomposed by the CEEMDAN method is similar to the theoretical modeling signal, which shows that CEEMADAN method has a good performance in decomposing complex rotor system signals.
3. Through CEEMDAN-CWT processing, the vibration signal of the rotor system itself is clearer, and the difference of 2X frequency between the cracked and healthy rotor systems is more obvious. At the rotating speed below 2000 rpm, the 2X frequency difference between cracked rotor and healthy rotor in CEEMDAN-CWT spectrum is about 1, while the difference of FFT spectrum of original signal is about 0.6, which shows that CEEMDAN-CWT can better judge the difference between the two rotor systems. The characteristics of the experimental cracked rotor can be better identified and have a good similarity with the simulation results according to CEEMDAN-CWT method.
4. From the 3D CEEMDAN-CWT spectrum, the 2X frequency of healthy rotor will not change obviously with the increased speed, but the 2X frequency of cracked rotor will increase obviously. This is different from the situation that both of them increase with the rotating speed in FFT spectrum, which shows that this method eliminates interference and makes the measurement more accurate.

CRediT authorship contribution statement

Wenjie Zhou: Writing – original draft, Supervision, Software, Project administration, Funding acquisition, Conceptualization. **Xian Jin:** Writing – original draft, Visualization, Validation, Software, Methodology, Investigation, Data curation. **Lei Ding:** Validation, Investigation, Data curation. **Ji Ma:** Validation, Investigation, Data curation. **Huihao Su:** Validation, Investigation, Data curation. **An Zhao:** Writing – review & editing, Methodology.

Declaration of competing interest

The authors declare that they have no known competing financial interests or personal relationships that could have appeared to influence the work reported in this paper.

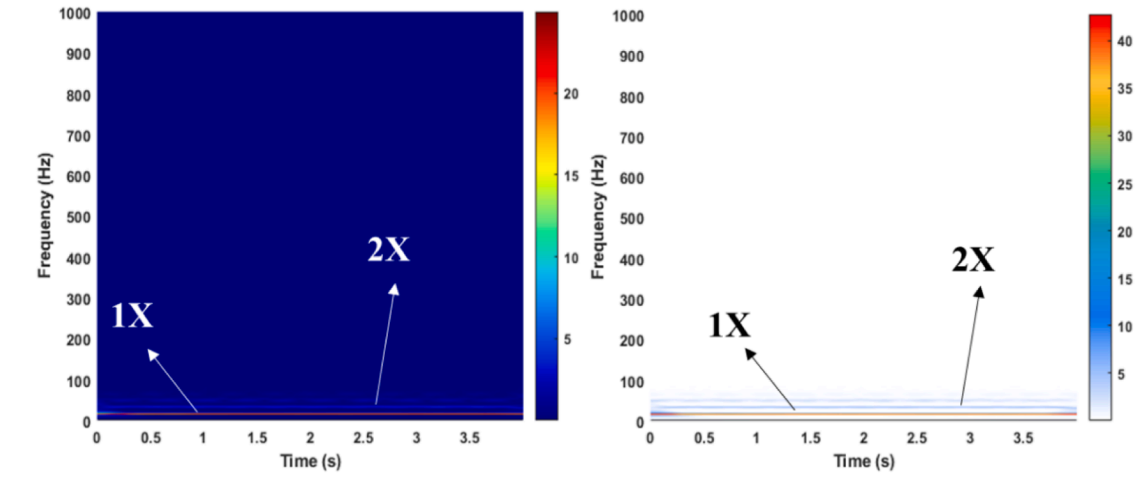

(a) 1000rpm (IMF8)

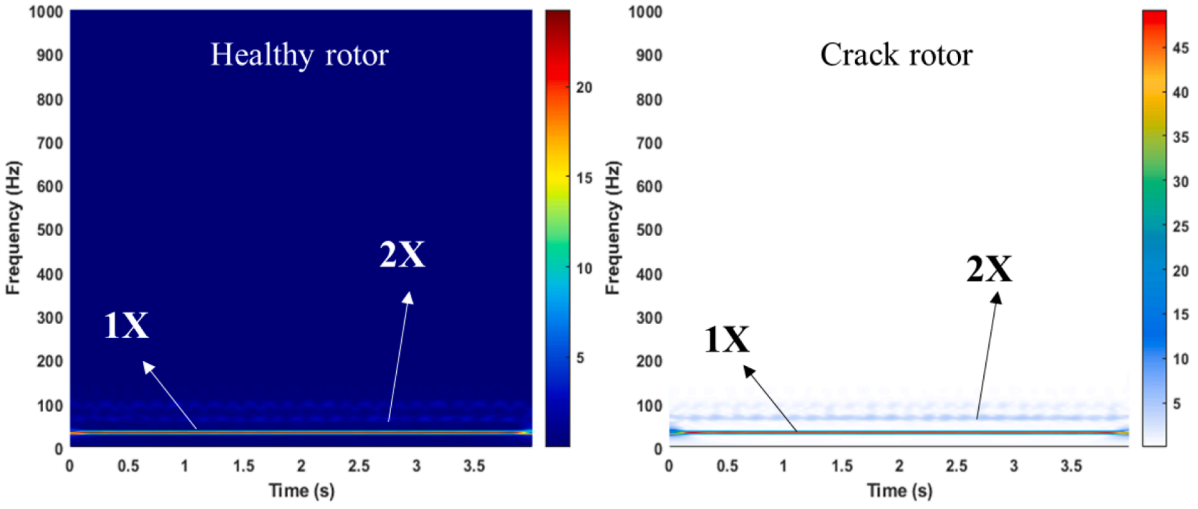

(b) 2000rpm (IMF7)

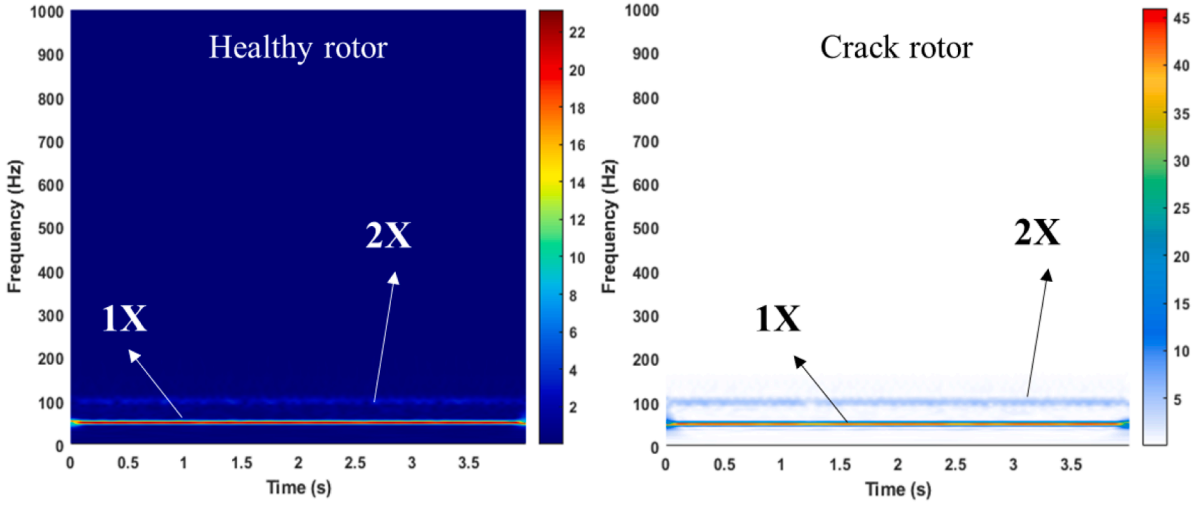

(c) 3000rpm (IMF7)

Fig. 16. Time domain signals of healthy rotor and cracked rotor with unbalanced mass processed by CEEMDAN-CWT.

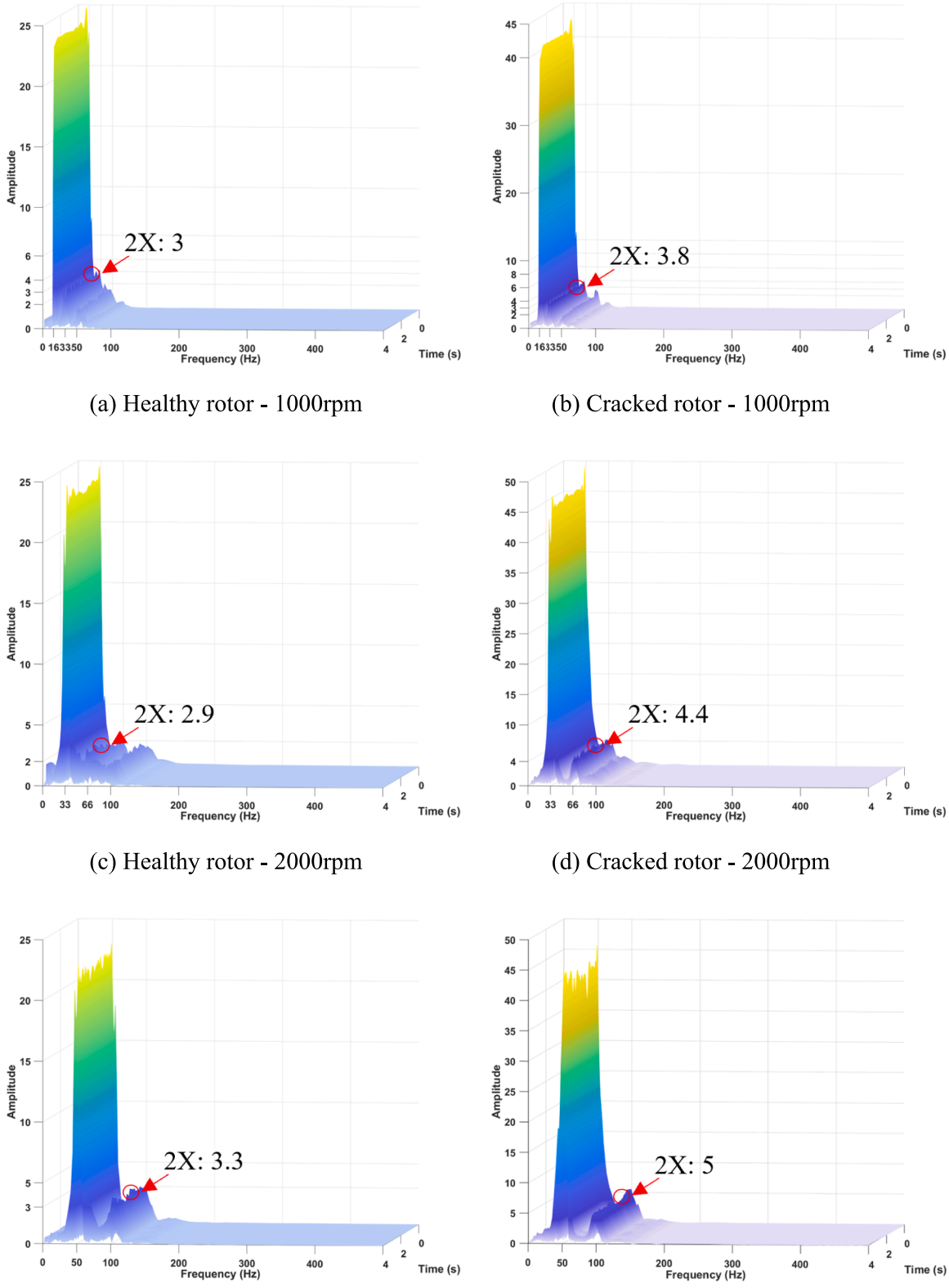

Fig 17. CEEMDAN-CWT spectrum of rotor vibration signal; 1000 rpm-IMF8; 2000 rpm-IMF7; 3000 rpm-IMF7.

Data availability

Data will be made available on request.

Acknowledgements

This work was supported by the National Natural Science Foundation of China (Grant No. 51706087), the Project funded by China Postdoctoral Science Foundation (Grant No. 2018 M642177) and the Zhejiang Postdoctoral Preferential Foundation (Grant No. zj2018009). The authors also thanks Jiangsu Lianyy Measurement & Control Technology Co., Ltd for experimental technical supports.

References

[1] Yang B, Martinez-Botas R, Yang M. Rotor flow-field timescale and unsteady effects on pulsed-flow turbocharger turbine. Aerosp Sci Technol 2022;120:107231. https://doi.org/10.1016/j.ast.2021.107231.
[2] Babu Rao K, Mallikarjuna Reddy D. Crack detection methodology in rotor bearing system by DWT based adaptive neuro-fuzzy inference systems. Appl Acoust 2022; 192:108728. https://doi.org/10.1016/j.apacoust.2022.108728.
[3] Zhi SD, Shen HK, Wang TY. Gearbox localized fault detection based on meshing frequency modulation analysis. Appl Acoust 2024;219:109943. https://doi.org/10.1016/j.apacoust.2024.109943.
[4] Sawalhi N, Ganeriwala S, Tóth M. Parallel misalignment modeling and coupling bending stiffness measurement of a rotor-bearing system. Appl Acoust 2019;144: 124–41. https://doi.org/10.1016/j.apacoust.2017.07.022.
[5] Wauer J. On the dynamics of cracked rotors: literature survey. Appl Mech Rev 1990;43:13–7. https://doi.org/10.1115/1.3119157.
[6] Gasch R. A survey of the dynamic behavior of a simple rotating shaft with a transverse crack. J Sound Vib 1993;160:313–32. https://doi.org/10.1006/jsvi.1993.1026.
[7] Dimarogonas AD. Vibration of cracked structures: a state of the art review. Eng Fract Mech 1996;55:831–57. https://doi.org/10.1016/0013-7944(94)00175-8.
[8] Jun OS, Eun HJ, Earmme YY, Lee CW. Modelling and vibration analysis of a simple rotor with a breathing crack. J Sound Vib 1992;155:273–90. https://doi.org/10.1016/0022-460x(92)90511-u.
[9] Darpe AK, Gupta K, Chawla A. Coupled bending, longitudinal and torsional vibrations of a cracked rotor. J Sound Vib 2004;269:33–60. https://doi.org/10.1016/s0022-460x(03)00003-8.
[10] Darpe AK, Gupta K, Chawla A. Transient response and breathing behaviour of a cracked Jeffcott rotor. J Sound Vib 2004;272:207–43. https://doi.org/10.1016/S0022-460X(03)00327-4.
[11] Al-Shudeifat MA, Butcher EA. New breathing functions for the transverse breathing crack of the cracked rotor system: approach for critical and subcritical harmonic analysis. J Sound Vib 2011;330:526–44. https://doi.org/10.1016/j.jsv.2010.08.022.
[12] Guo C, Al-Shudeifat MA, Yan J, Bergman LA, McFarland DM, Butcher EA. Stability analysis for transverse breathing cracks in rotor systems. Eur J Mech A/Solids 2013;42:27–34. https://doi.org/10.1016/j.euromechsol.2013. 04.001.
[13] Zhang B, Li Y. Six degrees of freedom coupled dynamic response of rotor with a transverse breathing crack. Nonlinear Dyn 2014;78:1843–61. https://doi.org/10.1007/s11071-014-1563-2.
[14] Spagnol J, Wu H, Yang C. Application of non-symmetric bending principles on modelling fatigue crack behaviour and vibration of a cracked rotor. Appl Sci 2020; 10:717. https://doi.org/10.3390/app10020717.
[15] Sinou JJ, Denimal E. Reliable crack detection in a rotor system with uncertainties via advanced simulation models based on kriging and Polynomial Chaos Expansion. Eur J Mech A/Solids 2022;92:104451. https://doi.org/10.1016/j.euromechsol.2021.104451.
[16] Kushwaha N, Patel VN. Nonlinear dynamic analysis of two-disk rotor system containing an unbalance influenced transverse crack. Nonlinear Dyn 2023;111: 1109–37. https://doi.org/10.1007/s11071-022-07893-7.
[17] El Arem S. Nonlinear analysis, instability and routes to chaos of a cracked rotating shaft. Nonlinear Dyn 2019;96:667–83. https://doi.org/10.1007/s11071-019-04813-0.
[18] El Arem S. On the mechanics of beams and shafts with cracks: A standard and generic approach. Eur J Mech A/Solids 2021;85:104088. https://doi.org/10.1016/j.euromechsol.2020.104088.
[19] Fu C, Ren XM, Yang YF, Lu K, Wang YL. Nonlinear response analysis of a rotor system with a transverse breathing crack under interval uncertainties. Int J Non Linear Mech 2018;105:77–87. https://doi.org/10.1016/j.ijnonlinmec.2018.07.001.
[20] Fu C, Xu YD, Yang YF, Lu K, Gu FS, Ball A. Dynamics analysis of a hollow-shaft rotor system with an open crack under model uncertainties. Commun Nonlinear Sci Numer Simul 2020:83. https://doi.org/10.1016/j.cnsns.2019.105102.
[21] Zhang Y, Xiang L, Hu SH, AJ, Yang X.. Dynamic analysis of composite rod fastening rotor system considering multiple parameter influence. Appl Math Model 2022; 105:615–30. https://doi.org/10.1016/j.apm.2022.01.010.
[22] Hou L, Chen Y, Cao Q, Lu Z. Nonlinear vibration analysis of a cracked rotor-ball bearing system during flight maneuvers. Mech Mach Theor 2016;105:515–28. https://doi.org/10.1016/j.mechmachtheory.2016.07.024.
[23] Vashisht RK, Peng Q. Crack detection in the rotor ball bearing system using switching control strategy and Short Time Fourier Transform. J Sound Vib 2018; 432:502–29. https://doi.org/10.1016/j.jsv.2018.06.061.
[24] Xiang L, Deng Z, Hu A. Multi-fault coupling study of a rotor system in experimental and numerical analyses. Nonlinear Dyn 2019;97:2607–25. https://doi.org/10.1007/s11071-019-05151-x.
[25] Xiang L, Zhang Y, Hu A, Ye F. Dynamic analysis and experiment investigation of a cracked dual-disc bearing-rotor system based on orbit morphological characteristics. Appl Math Model 2020;80:17–32. https://doi.org/10.1016/j.apm.2019.11.042.
[26] Darpe AK. A novel way to detect transverse surface crack in a rotating shaft. J Sound Vib 2007;305:151–71. https://doi.org/10.1016/j.jsv.2007.03.070.
[27] Gasch R. Dynamic behaviour of the Laval rotor with a transverse crack. Mech Syst Signal Process 2008;22:790–804. https://doi.org/10.1016/j.ymssp.2007.11.023.
[28] Sinou JJ, Lees AW. The influence of cracks in rotating shafts. J Sound Vib 2007; 285:1015–37. https://doi. org/10.1016/j.jsv.2004.09.008 49.
[29] Sinou JJ, Lees AW. A non-linear study of a cracked rotor. Eur J Mech A/Solids 2007;26:152–70. https://doi.org/10.1016/j.euromechsol.2006.04.002.
[30] Al-Shudeifat MA. On the finite element modeling of the asymmetric cracked rotor. J Sound Vib 2013;332:2795–807. https://doi.org/10.1016/j.jsv.2012.12.026.
[31] Guo C, Al-Shudeifat MA, Yan J, Bergman LA, D. McFarland M, Butcher EA. Application of empirical mode decomposition to a Jeffcott rotor with a breathing crack. J Sound Vib. 2013; 332: 3881—3892. https://doi.org/10. 1016/j.jsv.2013.02.031.
[32] Guo CZ, Yan JH, Bergman LA. Experimental dynamic analysis of a breathing cracked rotor. Chin J Mech Eng 2017;30:1177–83. https://doi.org/10.1007/s10033-017-0180-7.
[33] Lu Z, Lv Y, Ouyang H. A super-harmonic feature-based updating method for crack identification in rotors using a kriging surrogate model. Appl Sci 2019;9:2428. https://doi.org/10.3390/app9122428.
[34] Lei Y, Lin J, He Z, Zuo MJ. A review on empirical mode decomposition in fault diagnosis of rotating machinery. Mech Syst Signal Process 2013;35:108–12. https://doi.org/10.1016/j.ymssp.2012.09.015.
[35] Chen S, Huo X, Zhao H, Yao Y. Axial unbalance identification of GyroWheel rotor based on multi-position calibration and CEEMDAN-IIT denoising. Measurement 2021;183:109852. https://doi.org/10.1016/j.measurement.2021.109852.
[36] Hu Y, Yi O, Wang Z, Yu H, Liu L. Vibration signal denoising method based on CEEMDAN and its application in brake disc unbalance detection. Mech Syst Signal Process 2023;187:109972. https://doi.org/10.1016/j.ymssp.2022.109972.
[37] Li Z, Wang QS, Qin B, Shao W. Vibration characteristic analysis of flexible rotor-bearing system subjected to external combined loads. Eur J Mech A/Solids 2022; 96:104688. https://doi.org/10.1016/j.euromechsol.2022.104688.
[38] Liu J, Tang CK, Wu H, Xu ZD, Wang LF. An analytical calculation method of the load distribution and stiffness of an angular contact ball bearing. Mech Mach Theor 2019;142:103597. https://doi.org/10.1016/j.mechmachtheory.2019.103597.
[39] Lu Z, Dong D, Ouyang H, Cao S, Hua C. Localization of breathing cracks in stepped rotors using super-harmonic characteristic deflection shapes based on singular value decomposition in frequency domain. Fatigue Fract Eng Mater Struct 2017;40: 1825–37. https://doi.org/10.1111/ffe.12601.
[40] Tada H, Paris PC, Irwin GR. The Stress Analysis of Cracks Handbook. 3rd edn. New York: ASME Press; 2000.
[41] Darpe AK. Coupled vibrations of a rotor with slant crack. J Sound Vib 2007;305: 172–93. https://doi.org/10.1016/j.jsv.2007.03.079.
[42] Harris TA, Kotzalas MN. Rolling bearing analysis: essential concepts of bearing technology. CRC Press Boca Raton 2007.
[43] Jones A. General theory for elastically constrained ball and roller bearings under arbitrary load and speed conditions. ASME Trans J Basic Eng 1960;82:309–20. https://doi.org/10.1016/0043-1648(60)90271-4.
[44] Torres ME, Colominas MA, Schlotthauer G, Flandrin P. A complete ensemble empirical mode decomposition with adaptive noise. In: 2011 IEEE International Conference on Acoustics, Speech and Signal Processing; 2011. p. 4144–7. https://doi.org/10.1109/ICASSP.2011.5947265.
[45] Xu Y, Luo MZ, Li T, Song GB. ECG signal de-noising and baseline wander correction based on CEEMDAN and wavelet threshold. Sensors 2017;17:2754. https://doi.org/10.3390/s17122754.
[46] Colominas MA, Schlotthauer G, Torres ME, Flandrin P. Noise-assisted EMD methods in action. Adv Adapt Data Anal 2012;4:1–11. https://doi.org/10.1142/S1793536912500252.
[47] Spagnol JP, Wu H, Xiao K. Dynamic response of a cracked rotor with an unbalance influenced breathing mechanism. J Mech Sci Technol 2018;32:57–68. https://doi.org/10.1007/s12206-017-1207-9.
[48] Sinou JJ. An Experimental Investigation of Condition Monitoring for Notched Rotors Through Transient Signals and Wavelet Transform. Exp Mech 2009;49: 683–95. https://doi.org/10.1007/s11340-008-9193-6.
[49] Wang D, Cao HR, Yang Y, Du MG. Dynamic modeling and vibration analysis of cracked rotor-bearing system based on rigid body element method. Mech Syst Signal Process 2023;191:110152. https://doi.org/10.1016/j.ymssp.2023.110152.